Monthly Notices of the ROYAL ASTRONOMICAL SOCIETY

MNRAS **482,** 2422–2441 (2019) doi:10.1093/mnras/sty2779
Advance Access publication 2018 October 24

On the nature and physical conditions of the luminous Ly α emitter CR7 and its rest-frame UV components

David Sobral [1,2]★ Jorryt Matthee,[2] Gabriel Brammer,[3] Andrea Ferrara,[4,5] Lara Alegre,[6] Huub Röttgering,[2] Daniel Schaerer,[7,8] Bahram Mobasher[9] and Behnam Darvish[10]

[1]*Department of Physics, Lancaster University, Lancaster LA1 4YB, UK*
[2]*Leiden Observatory, Leiden University, PO Box 9513, NL-2300 RA Leiden, The Netherlands*
[3]*Space Telescope Science Institute, 3700 San Martin Dr, Baltimore MD 21211, USA*
[4]*Scuola Normale Superiore, Piazza dei Cavalieri 7, I-56126 Pisa, Italy*
[5]*Kavli IPMU, The University of Tokyo, 5-1-5 Kashiwanoha, Kashiwa 277-8583, Japan*
[6]*Institute for Astronomy, University of Edinburgh, Royal Observatory, Blackford Hill, Edinburgh EH9 3HJ, UK*
[7]*Observatoire de Genève, Université de Genève, 51 Ch. des Maillettes, CH-1290 Versoix, Switzerland*
[8]*CNRS, IRAP, 14 Avenue E. Belin, F-31400 Toulouse, France*
[9]*Department of Physics and Astronomy, University of California, 900 University Ave., Riverside, CA 92521, USA*
[10]*Cahill Center for Astrophysics, California Institute of Technology, 1216 East California Boulevard, Pasadena, CA 91125, USA*

Accepted 2018 October 10. Received 2018 October 3; in original form 2017 October 21

ABSTRACT

We present new *Hubble Space Telescope* (*HST*)/WFC3 observations and re-analyse VLT data to unveil the continuum, variability, and rest-frame ultraviolet (UV) lines of the multiple UV clumps of the most luminous Ly α emitter at $z = 6.6$, CR7 (COSMOS Redshift 7). Our re-reduced, flux-calibrated X-SHOOTER spectra of CR7 reveal an HeII emission line in observations obtained along the major axis of Ly α emission with the best seeing conditions. He II is spatially offset by $\approx+0.8$ arcsec from the peak of Ly α emission, and it is found towards clump B. Our WFC3 grism spectra detects the UV continuum of CR7's clump A, yielding a power law with $\beta = -2.5^{+0.6}_{-0.7}$ and $M_{\rm UV} = -21.87^{+0.25}_{-0.20}$. No significant variability is found for any of the UV clumps on their own, but there is tentative ($\approx$2.2 σ) brightening of CR7 in F110W as a whole from 2012 to 2017. *HST* grism data fail to robustly detect rest-frame UV lines in any of the clumps, implying fluxes $\lesssim 2 \times 10^{-17}$ erg s^{-1} cm^{-2} (3σ). We perform CLOUDY modelling to constrain the metallicity and the ionizing nature of CR7. CR7 seems to be actively forming stars without any clear active galactic nucleus activity in clump A, consistent with a metallicity of $\sim$0.05–0.2 Z$_\odot$. Component C or an interclump component between B and C may host a high ionization source. Our results highlight the need for spatially resolved information to study the formation and assembly of early galaxies.

Key words: galaxies: evolution – galaxies: high-redshift – galaxies: ISM – cosmology: observations – dark ages, reionization, first stars – early Universe.

1 INTRODUCTION

The significant progress in identifying large samples of distant galaxies (e.g. Bouwens et al. 2015; Harikane et al. 2018a,b; Sobral et al. 2018a) now enables detailed studies of the properties of the earliest stellar populations and black holes. Studies based on the ultraviolet (UV) slopes (β) of high-redshift galaxies indicate that they are consistent with little dust (e.g. Dunlop et al. 2012; Bouwens et al. 2014; Wilkins et al. 2016). However, results regarding the nature of the underlying stellar populations are ambiguous due to possible contributions from nebular continuum and dust–age–metallicity degeneracies (e.g. Raiter, Fosbury & Teimoorinia 2010; de Barros, Schaerer & Stark 2014); see also Popping, Puglisi & Norman (2017). These degeneracies can only be overcome by direct spectroscopic observations that trace different states of the interstellar medium, but such observations have so far been limited, due to the faintness of sources.

Bright targets from wide-field ground-based surveys (e.g. Bowler et al. 2014; Matthee et al. 2015; Hu et al. 2016; Santos, Sobral & Matthee 2016; Zheng et al. 2017; Jiang et al. 2017; Shibuya et al.

★ E-mail: d.sobral@lancaster.ac.uk

2018a) provide unique opportunities to obtain the first detailed and resolved studies of sources within the epoch of re-ionization. These bright sources are particularly suitable for follow-up with ALMA (e.g. Venemans et al. 2012; Ouchi et al. 2013; Capak et al. 2015; Maiolino et al. 2015; Smit et al. 2018; Carniani et al. 2018b). While some sources seem to be relatively dust free (e.g. Ota et al. 2014; Schaerer et al. 2015), consistent with metal-poor local galaxies, others seem to already have significant amounts of dust even at $z > 7$ (e.g. Watson et al. 2015). Interestingly, the majority of sources is resolved in multiple components in the rest-frame UV (e.g. Sobral et al. 2015; Bowler et al. 2017a; Matthee et al. 2017a) and/or in rest-frame far-infrared (FIR) cooling lines (e.g. Maiolino et al. 2015; Carniani et al. 2018a; Matthee et al. 2017b; Jones et al. 2017b).

In this paper, we study COSMOS Redshift 7 (CR7; $z = 6.604$, $L_{Ly\alpha} = 10^{43.8}$ erg s^{-1}; Sobral et al. 2015; hereafter S15), a remarkably luminous source within the epoch of re-ionization. CR7 was identified as a luminous Ly α candidate by Matthee et al. (2015), while its UV counterpart was independently found as a bright, but unreliable, $z \sim 6$ Lyman-break candidate (Bowler et al. 2012, 2014). CR7 was spectroscopically confirmed as a luminous Ly α emitter by S15 through the presence of a narrow, high Equivalent Width (EW) Ly α line (full width at half-maximum, FWHM $\approx$270 km s^{-1}; $EW_0 \approx 200$ Å). S15 estimated that its Ly α luminosity was roughly double of what had been computed in Matthee et al. (2015), due to the Ly α line being detected at $\sim$50 per cent transmission of the narrow-band filter used in Matthee et al. (2015).

One of the reasons that made CR7 an unreliable $z \sim 6$–7 candidate Lyman-break galaxy was the presence of an apparent *J* band excess of roughly $\sim 3\sigma$ (Bowler et al. 2012, 2014) based on UltraVISTA data release 2 (DR2) data (S15) and the strong Ly α contamination in the *z* band. The spectroscopic confirmation of CR7 as an Ly α emitter at $z = 6.6$ and the NIR photometry provided strong hints that an emission line should be contributing to the flux in the NIR. The shallow X-SHOOTER spectra of CR7 revealed an emission line in the *J* band ($EW_0 \gtrsim 20$ Å), interpreted as narrow HeII1640 Å ($v_{FWHM} = 130$ km s^{-1}), while no metal line was found at the current observational limits in the UV (S15). Such observations made CR7 unique, not only because it became the most luminous Ly α emitter at high redshift, but also due to being a candidate for a very low-metallicity starburst ('PopIII-like') or active galactic nucleus (AGN), particularly due to the high HeII/Ly $\alpha \approx$ 0.2 line ratio estimated from photometry. As discussed in S15, any 'normal' metallicity source would have been detected in CIV or CIII] (e.g. Stark et al. 2015a,b; Sobral et al. 2018b), indicating that the metallicity of CR7 should be very low (e.g. Hartwig et al. 2016). As the ionization energy of HeII is 54.4 eV, the ionizing source leading to HeII in CR7 must be very hot, with an expected effective temperature of $T \sim 10^5$K, hotter than normal stellar populations.

Due to its unique properties, CR7 has been discussed in several studies, some focusing on one of the hypotheses discussed in S15 that it could harbour a direct collapse black hole (DCBH, e.g. Pallottini et al. 2015; Agarwal et al. 2016, 2017; Hartwig et al. 2016; Smith, Bromm & Loeb 2016; Pacucci et al. 2017). However, as Dijkstra, Gronke & Sobral (2016) show, the DCBH interpretation has significant problems and realistically it cannot be favoured over e.g. PopIII-like (i.e. very low metallicity; e.g. Visbal, Haiman & Bryan 2016; Visbal, Bryan & Haiman 2017) stellar populations. Dijkstra et al. (2016) also argued that CR7's Ly α line is well explained by outflowing shell models, similarly to lower redshift Ly α emitters (e.g. Gronke 2017; Karman et al. 2017).

CR7 has been found to have a 3.6 μm excess, discussed as potential e.g. Hβ + [OIII]5007 emission for the source as a whole (Matthee et al. 2015; Bowler et al. 2017b; Harikane et al. 2018b). Recent studies went beyond the direct photometric analysis presented in S15 and deconvolved *Spitzer*/IRAC data (Agarwal et al. 2016; Bowler et al. 2017b), attempting to measure the properties of CR7's three different UV clumps. Such studies have reached similar observational results but often contradictory interpretations. For example, Bowler et al. (2017b) identify the brightest UV clump in CR7 (clump A) as the brightest at 3.6 μm and interprets such brightness as [OIII] 5007 emission, using it to argue for a very low-metallicity population with significant binary contribution, or a low-metallicity AGN. Others (e.g. Agarwal et al. 2017; Pacucci et al. 2017) argue that those are the signatures of a 'post-DCBH'. Bowler et al. (2017b) also note that CR7's *J* magnitude has changed by $\approx$+ 0.2 mag from the public DR2 data used in S15, which makes the spectral energy distribution (SED) signature for HeII based on photometry less significant. Shibuya et al. (2018b) presented spectroscopic results of luminous Ly α emitters, and analysed X-SHOOTER data for CR7 to reach the same conclusions as S15 regarding Ly α, but argue against the HeII line detection. More recently, [CII] was detected in each of CR7's clumps with ALMA (Matthee et al. 2017b, hereafter M17), with hints of a spectroscopically backed multiple major merger in CR7.

In this paper, we explore new *Hubble Space Telescope* (*HST*)/WFC3 resolved grism and imaging data, re-analyse and re-interpret previous spectroscopic data to further unveil the nature of CR7. In Section 2, we present the observations, data reduction, and re-analysis of spectroscopic data. Results are presented in Section 3. We use the best constraints on rest-frame UV emission lines and interpret them with our CLOUDY modelling in Section 4. We discuss the results in Section 5 and present the conclusions in Section 6. Throughout this paper, we use AB magnitudes (Oke & Gunn 1983), a Salpeter (1955) initial mass function (IMF), and a Λcold dark matter cosmology with $H_0 = 70$ km s^{-1} Mpc^{-1}, $\Omega_M = 0.3$, and $\Omega_\Lambda = 0.7$.

2 OBSERVATIONS OF CR7

2.1 Imaging observations and SFR properties from *HST* and ALMA

HST imaging reveals that CR7 consists of three UV 'clumps' (Sobral et al. 2015; Bowler et al. 2017a); see Fig. 1. We note that slit spectroscopic follow-up was targeted roughly at the peak of Ly α flux, and thus roughly at the position of clump A (see Fig. 1), but without knowing that the source could be resolved in three UV clumps (see S15). Therefore, clumps B and C were not originally spectroscopically confirmed even though they are within the Ly α halo as observed with the narrow-band data and have a Lyman break consistent with $z > 6$. Deep, high spatial and spectral resolution ALMA [CII] data have allowed to spectroscopically confirm each of the UV clumps A, B, and C as being part of the same system (M17). Readers are referred to M17 for a discussion on the spectroscopic confirmation of both clumps B and C and on the further dynamical and physical informations inferred from the ALMA data, including discussions on the extra [CII] component between clumps B and C ($M_{dyn} \sim 2 \times 10^{10}$ M$_\odot$; C-2 in M17) which is not seen in the UV (see also Carniani et al. 2018a).

Clump A, the brightest ($M_{UV} = -21.6 \pm 0.1$; M17), roughly coincides with the peak of Ly α emission and has a UV slope β (corrected for the contribution of Ly α to the F110W photometry) of $\beta = -2.3 \pm 0.4$ (measured within a 1 arcsec diameter aperture; M17). Clumps B and C are fainter ($M_{UV} = -19.8 \pm 0.2$ and

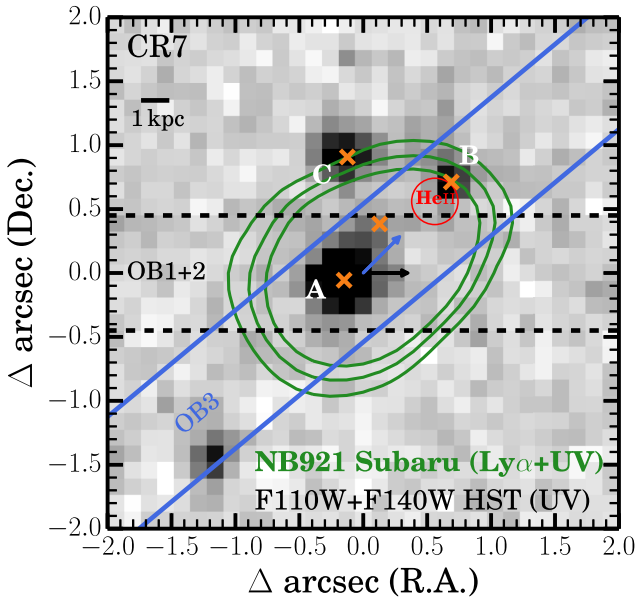

Figure 1. The *HST*/WFC3 stacked image showing the rest-frame UV (contrast cut-offs: -1σ and 5σ), and the NB921 ground-based Lyα contours (3σ, 4σ, and 5σ) of CR7 (Matthee et al. 2015; Sobral et al. 2015). We also show the approximate position, rotation and on-sky width (0.9 arcsec) of the X-SHOOTER slit used for the three OBs (see Section 2.2). The two arrows point towards positive spatial locations in the reduced 2D spectra, i.e. positive offsets in the *Y* coordinate of the reduced 2D spectra (see e.g. Fig. 2). The location of HeII detected in OB3 is also indicated based on the 0.8 arcsec offset from the central position, making it consistent with being towards clump B but not on top of the UV clump. The orange crosses indicate the positions we use to place apertures on individual clumps or for the full system.

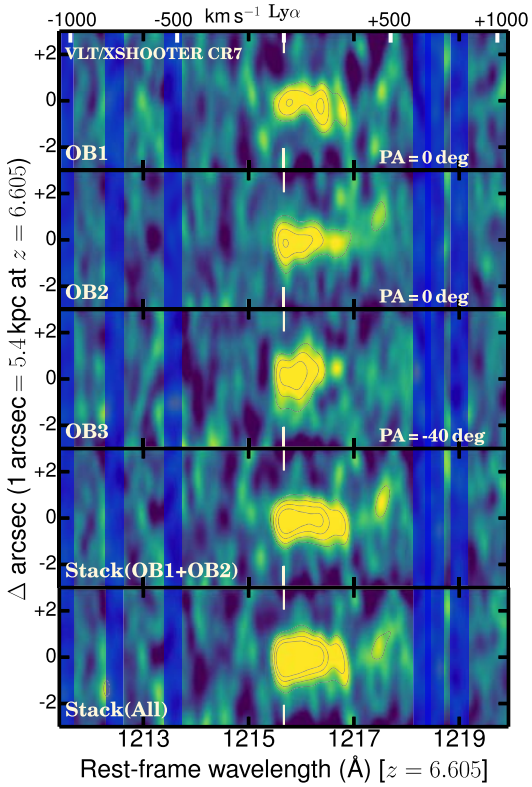

Figure 2. Our reduced and flux-calibrated 2D X-SHOOTER spectra, zoomed-in at Lyα, in S/N space showing 2σ, 3σ, 4σ, and 5σ contours after smoothing with a 3 spectral–spatial pixel Gaussian kernel. The location of sky lines are shown, even though all these are relatively weak. OB1 and OB2 were done consecutively on the same night but OB2 resulted from a better acquisition of the offset star; both were done under variable seeing. OB3 was done with a different slit angle, sampling along the axis of clumps A and B (see Fig. 1) and under better and more stable seeing conditions.

-20.1 ± 0.1, respectively; Fig. 1) and show $\beta = -1.0 \pm 1.0$ and -2.3 ± 0.8 in 0.4 arcsec apertures (see also Bowler et al. 2017b). As the UV slopes are quite uncertain, they allow for large dust attenuations and hence uncertain SFRs. However, as shown in M17, constraints on the IR continuum luminosity from very deep ALMA observations of CR7 can mitigate these uncertainties. In practice, as CR7 is undetected in dust continuum, it implies a relatively low FIR luminosity of $L_{\rm IR}(T_{\rm d} = 35\,{\rm K}) < 3.1 \times 10^{10}\,{\rm L}_{\odot}$ and a dust mass $M_{\rm dust} < 8.1 \times 10^{6}\,{\rm M}_{\odot}$ (3σ limits). Such limits imply a maximum dust-obscured star formation rate of $<5.4\,{\rm M}_{\odot}\,{\rm yr}^{-1}$ for the full system. Overall, the combination of *HST* and ALMA observations reveal dust-corrected ${\rm SFR}_{\rm UV+IR} = 28^{+2}_{-1}$, 5^{+2}_{-1}, and $7^{+1}_{-1}\,{\rm M}_{\odot}\,{\rm yr}^{-1}$ (see M17) for clumps A, B, and C, respectively, for a Salpeter IMF (and a factor ≈1.8 lower for a Chabrier IMF). The SFR of the full CR7 system (A,B,C) is $45^{+2}_{-2}\,{\rm M}_{\odot}\,{\rm yr}^{-1}$, taking into account the ALMA constraints for obscured SFR.

2.2 Re-analysis of X-SHOOTER observations

We re-analyse the X-SHOOTER data originally presented in S15. The NIR spectroscopic data in S15 were flux-calibrated using public DR2 UltraVISTA *J*-band photometry. Those public data revealed a strong *J*-band excess for CR7 (S15). More recently, Bowler et al. (2017b) used DR3 data to measure a fainter *J*-band magnitude, due to a change from DR2 to DR3 in the public UltraVISTA *J*-band photometry. We investigate such potential change in UltraVISTA *J*-band data separately in Section 3.2.

The VLT/X-SHOOTER data were obtained over three different observing blocks (OBs; see Fig. 1) of about 1 h each, with two OBs obtained on 2015 January 22 (seeing 1.2 arcsec; varying from 0.8 to 1.6 arcsec) and a final OB (a repeat of OB1, which we name OB3 in this paper, but that is formally called 'OB1' in the ESO archive). OB3 was obtained with a seeing of 0.8 arcsec, varying from 0.7 to 0.9 arcsec, and thus in better conditions than OBs 1 and 2 and was done on 2015 February 15. We reduce all OBs separately. All OBs used a 0.9 arcsec slit in both the VIS and NIR arms.

For the first two OBs a PA angle of 0 deg was used (see Fig. 1), together with an acquisition source at 10:01:03.156, +01:48:47.89. Offsets of −77.27 arcsec (RA) and −32.63 arcsec (Dec.) were used to offset from the acquisition source to CR7. The acquisition for the first OB (OB1, 2015 January 22) was suspected to be relatively off-target due to an unreliable acquisition star centring (acquisition star was not centred in the slit), leading to an apparent lower Lyα flux and a spatially truncated and complex/double-peaked Lyα profile, different from that found in the OB2 which was done with a good acquisition and with Keck/DEIMOS data (see Fig. 2 and S15). When repeating OB1 and in order to avoid problems with acquisition, another acquisition source was used: 10:01:00.227, 01:48:42.99, applying an offset of −33.34 arcsec (RA) and −27.74 arcsec (Dec.) and this time with a PA angle of −39.°76, in order to align the slit

with the elongation of the Ly α 2D distribution obtained from the narrow-band imaging[1] (Fig. 1).

We use the X-SHOOTER pipeline (v2.4.8; Modigliani et al. 2010), and follow the steps fully described in Matthee et al. (2017a) and Sobral et al. (2018b), including flux calibration. We note that our data reduction results in a significantly improved wavelength calibration in the NIR arm when compared to S15, which we find to be off by -6.9 ± 0.6 Å (λ_{air}) in the NIR arm when compared to our reduction[2]; this is obtained by matching OH lines (see Fig. A1). We find this offset to be due to the use of old arcs in S15. The latest ESO public reduction and Shibuya et al. (2018b) obtain the same wavelength calibration as using the most up-to-date pipeline. In the VIS arm, we find no significant differences in the wavelength calibration when comparing to S15, but we now flux calibrate the data (using appropriate telluric stars) without relying on any narrow- or broad-band photometry, unlike S15. In Fig. 2, we show the reduced 2D spectra centred on Ly α for each individual OB (note that the positive spatial direction is indicated with an arrow in Fig. 1). We also show the combined stack of the three OBs and when combining only the 2 first OBs which trace a different spatial region when compared to OB3. We present the results in Section 3.1.

Our reduced spectra show a spectral resolution (FWHM based on sky lines) of $\approx$1.6 Å at $\approx$9000 Å ($\approx$55 km s^{-1}), corresponding to $R \sim 5600$ and $\approx$3.5 Å at $\approx$ 16 000 Å ($\approx$65 km s^{-1}), corresponding to $R \sim 4600$. In order to improve the signal-to-noise ratio and reduce noise spikes and prevent the dominance of individual pixels, we bin our 1D spectra to one-third of the resolution by using bins of 0.6 Å in the VIS and 1.2 Å in the NIR arm. We use these 1D spectra converted to λ_{vacuum} throughout our analysis unless noted otherwise. The analysis is done following Sobral et al. (2018b) using Monte Carlo (MC) forward modelling to search for emission lines and measure the uncertainties. We provide further details in relevant sections throughout the manuscript.

2.3 Re-analysis of SINFONI observations

We also re-reduce the SINFONI data presented in S15. The final data cube in S15 was produced with equal weights for all exposures by using the SINFONI pipeline to reduce all the OBs together with a single set of calibration observations. The data were scaled using the *J* magnitude from UltraVISTA and the flux implied for HeII from UltraVISTA. Finally, the stack was combined with X-SHOOTER data which had a systematic offset in wavelength of 6.9 Å, as stated in Section 2.2.

CR7 was observed with SINFONI in 2015 March and April (program 294.A-5039) with six different OBs of about 1 h each. Four of those OBs were classed A (highest quality), one of them was classed B (seeing >1 arcsec) and another one was classed C (bad quality, due to clouds). Here, we neglect the one classed C.

We use the SINFONI pipeline v.2.5.2 and implement all the steps using ESOREX. We reduce each OB with the appropriate specific calibration files, done either on the same night or on the closest night possible. We reduce each OB individually, along with each standard/telluric star. In total, five different telluric stars were observed, one per OB/night of observations, and we reduce those observations in the same way as the science observations. In order to flux calibrate, we use 2MASS *JHK* magnitudes of each star. We extract the standard stars' spectra by obtaining the total counts per wavelength (normalized by exposure time) in the full detector, following the procedure in the pipeline, and we then re-extract them over the apertures used to extract the science spectra. This allows us to derive aperture corrections which vary per OB (due to seeing), which are typically $\sim$1.5 for 1.4 arcsec extraction apertures, and $\sim$1.2 for 2 arcsec aperture extractions.

We find that the absolute astrometry of the pipeline reduced data cubes is not reliable, as each OB (which is done with the same offset star and with the same jitter pattern) results in shifts of several arcseconds between each reduced data cube. We attempt to extract spectra in the RA and Dec. positions of CR7 assuming the astrometry is correct but fail to detect any signal, with the stacked spectra resulting in high noise levels due to the extraction away from the centre. Finally, we make the assumption that the data cubes are centred at the position of the first exposure which serves as reference for the stack of each OB, and extract 1D spectra per OB with apertures of 0.9, 1.4, and 2 arcsec (using our aperture corrections), which we assume are centred at the peak of Ly α emission and will be able to cover the full CR7 system. In order to improve our sky subtraction, we compute the median of 1000 empty apertures with the same size as the extraction aperture and subtract it from the extraction aperture. We also use the 1000 apertures per spectral element to compute the standard deviation and use it as the noise at that specific wavelength. Finally, we stack spectra from the different OBs by weighting them with the inverse of the variance (σ^2). Reduced SINFONI spectra have a resolution (FWHM, based on OH lines) of $\sim$6.4 Å at $\sim$1.2 μm ($R \sim 1900$; $\sim$150 km s^{-1}). When binned to one-third of the resolution, the spectra (0.9 arcsec apertures, stacked) reach a 1σ flux limit of $\approx 5 \times 10^{-19}$ erg s^{-1} cm^{-2} Å^{-1} away from OH sky lines at an observed $\lambda \approx 1.245$ μm.

2.4 WFC3/*HST* grism observations

We observed CR7 with the WFC3 grism with GO program 14495 (PI: Sobral). Observations were conducted over a total of five orbits: two orbits during 2017 January 21 and 3 further orbits conducted during 2017 March 17. We used two different PA angles (252°.37 and 322°.37; see Fig. 3), each calculated to avoid significant contamination by nearby bright sources and in order to investigate the spectra of the rest-frame UV components A, B, and C separately.

For each orbit, we obtained an image with the F140W filter, two grism observations (dithered) with the G141 grating (central wavelength 13886.72 Å), and another image after the second grism observation. These allow us to correctly identify the sources and to clearly locate the rest-frame UV clumps A, B, and C within CR7. The F140W images were obtained at the start and end of each orbit with the aim to minimize the impact of variable sky background on the grism exposure (due to the bright Earth limb and the He 1.083 μm line emission from the upper atmosphere; see Brammer et al. 2014). A four-point dithering pattern was used to

[1] At the time of preparation of all spectroscopic observations of CR7 in 2014 and early 2015 (and the multiwavelength analysis) the resolved nature of CR7, only revealed by *HST* data in 2015 April, was unknown.

[2] It is important to note that in the literature λ_{air} can be used instead of λ_{vacuum} and that HeII is sometimes used as 1640.0 Å instead of 1640.47 Å in vacuum; these can combine to lead to multiple offsets between different studies. Such small differences are typically negligible at lower redshift and for low-resolution spectra, but they become important at high redshift and for high-resolution spectra, as they can lead to significant discrepancies and offsets.

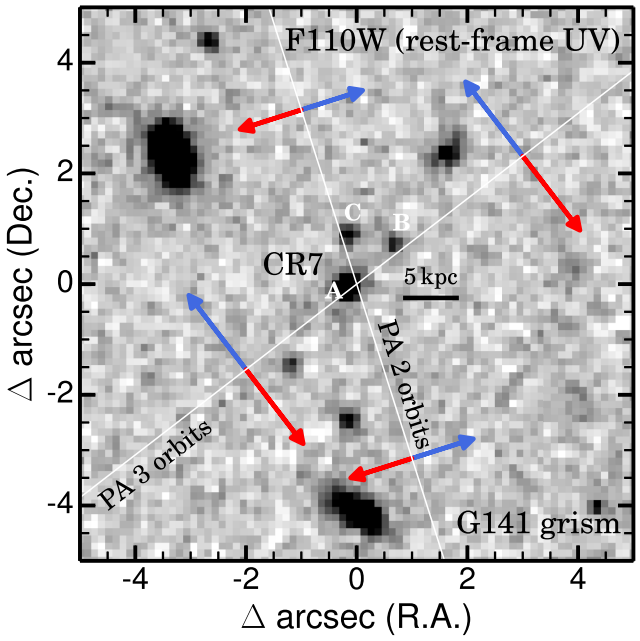

Figure 3. *HST*/WFC3 F110W ($Y + J$) image centred on CR7 and the immediate surroundings for our G141 grism observations. We indicate the PA angles used for each of the two visits done: one observing for two orbits and the final one observing for three orbits. We also indicate the dispersion direction and the direction in which bluer/redder light gets dispersed once the grism is used to take observations. Our observations allow us to avoid contamination from nearby sources and obtain spectra for each of the components A, B, and C for CR7. We also show the 5 kpc scale at $z = 6.6$.

improve the sampling of the point spread function and to overcome cosmetic defects of the detector.

We obtained imaging exposures of 0.25 ks and grism exposures of 1.10 ks. Our total exposure grism time with G141 is 11.0 ks. For a full description of the calibration of the WFC3/G141 grism, see e.g. Kuntschner et al. (2010).

2.4.1 *Data reduction and extraction*

We reduce the data following Brammer et al. (2012). The grism data were reduced using the grism reduction pipeline developed by the 3D- HST team (e.g. Brammer et al. 2012; Momcheva et al. 2016). The main reduction steps are fully explained in Momcheva et al. (2016). In summary, the flat-fielded and global background-subtracted grism images are interlaced to produce 2D spectra for each of the UV clumps A, B, and C, independently. We also identify any potential contamination from faint and/or nearby sources and subtract it when we extract the 1D spectra. Our reduced data show a resolution of $R \sim 100$ (FHWM 150 Å) at $\lambda \sim 1.2\,\mu$m ($\approx$3750 km s^{-1}), and thus a resolution of $\sim$20 Å at $\sim$1600 Å rest frame for CR7 ($z = 6.6$). We bin the data to one-third of the resolution ($\approx$50 Å, observed). We note that the *HST*/WFC3 grism resolution is $\approx$40 times worse than X-SHOOTER at $\lambda \sim 1.2\,\mu$m.

We extract the spectra of the three major components of CR7 from their central positions by using the rest-frame UV continuum images obtained with *HST*. We see clear continuum in the 2D spectrum for clump A (the brightest) and weak continuum from B. We find that apart from some minor contamination at observed $\lambda \sim 15500$–15700 Å, the spectra of the three clumps of CR7 are not contaminated by any other nearby sources, as expected from our observing planning (Fig. 3). We thus estimate the noise on the CR7 spectrum by extracting spectra in a range of spatial locations (per clump) with similarly low contamination. We use the standard deviation per wavelength as the estimate of our 1σ error and we use these to quantify the signal-to-noise ratio (S/N) and to evaluate the significance of both the continuum and the detection of any emission lines. Our 1D spectra for the extraction of the three components of CR7 show an average noise level of $(3.1-3.4) \times 10^{-19}$ erg s^{-1} cm^{-2} Å^{-1} for $1.1 < \lambda_{\rm observed} < 1.6\,\mu$m.

3 RESULTS

3.1 VLT spectroscopy

3.1.1 *Ly α in X-SHOOTER*

In Fig. 2, we show the 2D spectra for our re-analysis of the X-SHOOTER data, in an S/N scale, focusing on Ly α. We find potential variations in the Ly α profile, indicating that we may be probing different spatial regions within the source. This is likely due to the bad acquisition for OB1 (in comparison to OB2; both OBs were done with variable seeing of $\sim$1.2 arcsec) and due to a different acquisition star and PA angle for OB3. Even though the S/N is not high enough for a robust conclusion, OB3 suggests a redshifted component of Ly α in the direction of clump B (see Fig. 1). As can be seen in more detail in Fig. 4, OB3 reveals a narrower Ly α profile ($\sim$180 km s^{-1}) than OB2 ($\sim$310 km s^{-1}), hinting that the Ly α FWHM may be narrower along the major axis of Ly α (running from A to B), but both OB2 and OB3 show the same/similar blue cut-off. In order to quantify any differences in the Ly α profile, we perform an MC simulation, perturbing each spectral element in the 1D spectra (one-third of the resolution) within its Gaussian distribution uncertainty independently. We do this 10 000 times (following the methodology in Sobral et al. 2018b) and each time we measure the FWHM of the Ly α line by fitting a Gaussian and deconvolve it with the resolution. Results are given in Table 1. We find that OB1 and OB2 yield Ly α FWHMs of 290^{+62}_{-45} and 310^{+95}_{-67} km s^{-1}, respectively, while for OB3, we obtain a narrower Ly α profile of 177^{+44}_{-30} km s^{-1} and for the stack of all OBs we obtain 270^{+35}_{-30} km s^{-1}, in agreement with S15. Our results suggest that there may be a difference between the profile of Ly α between a PA angle of 0 (tracing just clump A) and a PA angle of -40 that connects clumps A and B. Such differences between OB1 or OB2 and OB3 are only significant at the 1.7σ–1.8σ level individually, but the difference between OB3 and the stack of OB1 and OB2 is at the $\approx 3\sigma$ level. Deeper data are needed to fully confirm these potential spatial differences in the Ly α profile.

Interestingly, M17 finds that the axis perpendicular to the Ly α major axis shows the largest velocity shift in [CII], from the most blueshift towards C to the highest redshift towards the opposite direction, and with a total velocity shift of $\sim$300 km s^{-1}, similar to the Ly α FWHM in OB2 (Fig. 4). It may well be that Ly α itself is tracing complex dynamics, or that we are seeing more complex radiation transfer effects or different HI column densities. Deep observations with MUSE on the VLT and further modelling (e.g. Gronke 2017; Matthee et al. 2018) will robustly clarify the current open scenarios.

3.1.2 *HeII in X-SHOOTER*

We show our re-analysis of X-SHOOTER data, split by OB, in Fig. 5, where we present the extracted 1D spectra at the expected

Table 1. Results of our MC measurements of X-SHOOTER CR7 spectra (following Sobral et al. 2018b). The results present the median values of fluxes (median of the integrated Gaussian fluxes) and the 16th and 84th percentiles as the lower and upper errors. We also present similar values for the FWHM, deconvolved for resolution (FWHM) from all Gaussian fits per line. For OB1, OB2, and the stack of those OBs, HeII is not detected above 2.5σ and we provide the derived 99.4 percentile (<2.5σ) as an upper limit, but also provide the median fluxes and 16th and 84th percentiles (in brackets) for comparison. No slit corrections are applied for these specific measurements but note that such corrections are particularly important for the Lyα line which is spatially extended beyond what the slit captures.

Spectra OBs/Stack	PA angle (deg)	$F_{Ly\alpha}/10^{-17}$ (erg s^{-1} cm^{-2})	$FWHM_{Ly\alpha}$ (km s^{-1})	$F_{HeII}/10^{-17}$ (erg s^{-1} cm^{-2})	$FWHM_{HeII}$ (km s^{-1})
OB1	0	$4.8^{+0.7}_{-0.7}$	290^{+62}_{-45}	<7.8 ($1.8^{+2.5}_{-2.0}$)	–
OB2	0	$5.9^{+1.0}_{-1.0}$	310^{+95}_{-67}	<5.3 ($0.8^{+1.0}_{-0.8}$)	–
OB3	−40	$4.4^{+0.8}_{-0.6}$	177^{+44}_{-30}	$3.4^{+1.0}_{-0.9}$	210^{+70}_{-83}
Stack (OB1+OB2)	0	$5.8^{+0.7}_{-0.6}$	350^{+56}_{-40}	<4.1 ($0.8^{+0.9}_{-0.8}$)	–
Stack (all)	0−40	$5.2^{+0.5}_{-0.4}$	270^{+35}_{-30}	$2.0^{+0.6}_{-0.6}$	330^{+113}_{-120}

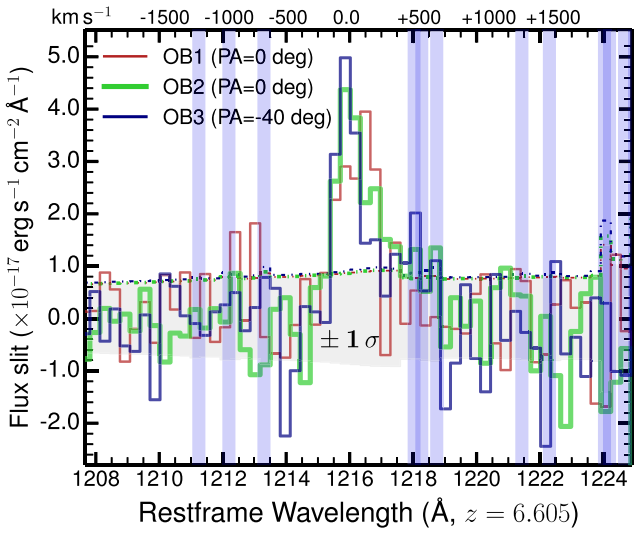

Figure 4. The extracted 1D spectra from X-SHOOTER at the position of Lyα showing results from different OBs which trace different spatial scales and different angles for CR7 (see Fig. 1). We show spectra binned by 75 km s^{-1}. We find that OB3, that traces along the Lyα major axis, connecting A to B, shows the highest flux peak and the narrowest Lyα profile, with an FWHM of 180^{+40}_{-30} km s^{-1}. Both OB1 and OB2, obtained with a 0° PA angle show a broader Lyα profile than OB3. The differences between OB1 or OB2 and OB3 are only significant at the 1.7σ − 1.8σ level individually, but the stack of OB1 and OB2 yields an Lyα FWHM which is ≈3σ away from that of OB3 (see Table 1).

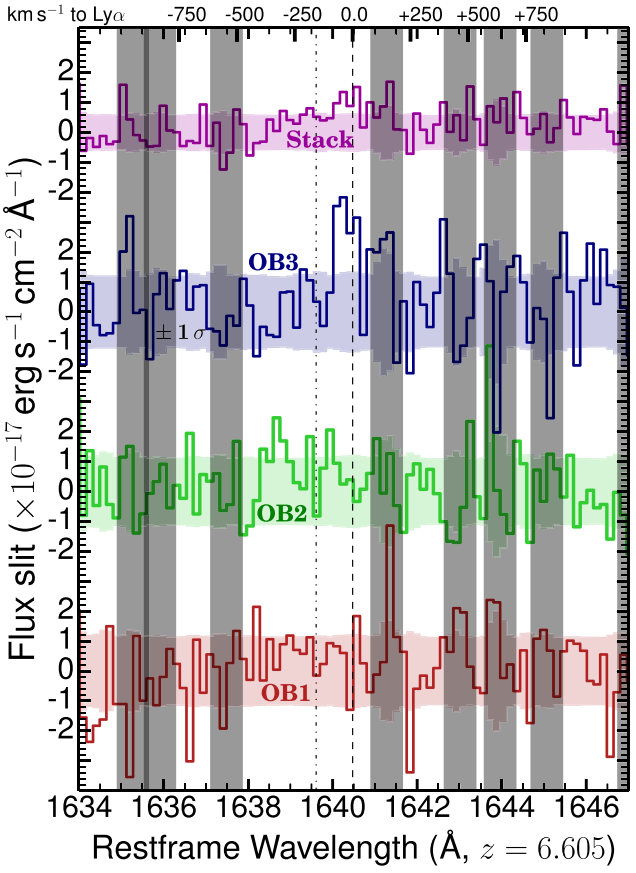

Figure 5. The extracted 1D spectra from our X-SHOOTER re-analysis of individual OBs and the full stack at the expected location of HeII. OH lines are clearly labelled. We find no significant HeII detection for CR7 in the spatial locations covered by OB1 and OB2. OB3 reveals a significant HeII detection (which dominates the signal in S15), explaining the detection in the full stack. We show the expected location of the HeII line in the case of no velocity shift from Lyα and also where we would expect to detect based on [CII]-ALMA emission from clump A (dotted–dashed). We find that the HeII signal is consistent with a relatively small velocity offset from Lyα of ∼100 km s^{-1}, although we note that the line is spatially coincident in OB3 with a redshifted Lyα component.

rest-frame wavelength of HeII at $z = 6.605$. The results of our MC analysis for OB3 and a comparison to S15 are shown in Fig. 6. The full results for all OBs and stacks are presented in Table 1. We also present the 2D spectrum per OB in Fig. 7.

Our re-analysis is able to recover the HeII emission line detected in S15, but we can show that the signal is coming from OB3[3] (see Figs 5–7). Based on OB3 only, we detect HeII at a ≈3.8σ level with a flux of $3.4^{+1.0}_{-0.9} \times 10^{-17}$ erg s^{-1} cm^{-2} (see Table 1).[4] The 2D spectra

[3]OB3 was observed with the best, most stable seeing and with the slit aligned with the major axis of the Lyα extent. OB3 also shows the highest Lyα flux peak (Fig. 4) and the narrowest Lyα profile.

[4]Simply placing an aperture in the 2D spectra of OB3 without any binning or smoothing leads to a flux of ≈3×10^{-17} erg s^{-1} cm^{-2}.

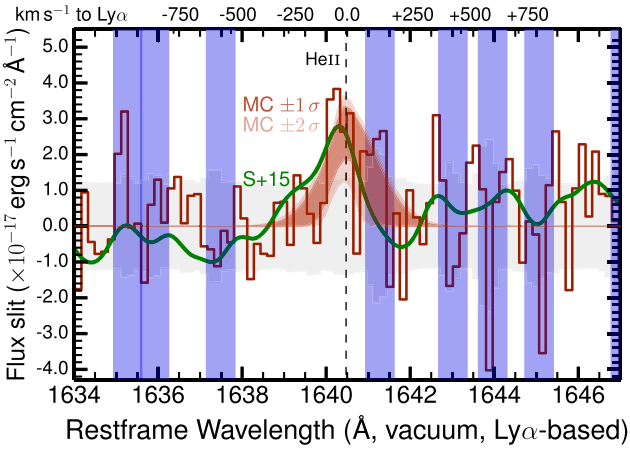

Figure 6. The spectrum of CR7 for OB3, along a PA angle of -40° and extracted centred on the signal in the NIR, 0.8 arcsec away from the peak brightness of Lyα towards clump B. We show the results of our forward modelling MC analysis, by perturbing the spectrum 10 000 times and the range of fits encompassing $\pm1\sigma$ and $\pm2\sigma$. We also show the location of OH/sky lines. As a comparison, we show the 1D spectra presented in S15, shifted in wavelength by +6.9 Å and converted to vacuum and arbitrarily normalized in flux for comparison. The signal in S15 is consistent with being dominated by OB3, but it is smoothed with a wide Gaussian kernel and also by masking sky lines before smoothing.

of OB3 also shows negatives up and down from the offsets along the slit[5] (Fig. 7). These are typically taken as clear indications that an emission line is real. The detected HeII line in OB3 has a measured FWHM of 210^{+70}_{-80} km s^{-1}, consistent with measurements from S15 (see Fig. 6). The HeII FWHM is statistically consistent within $1\,\sigma$ with the Lyα FWHM in OB3 (see Table 1). The HeII signal from OB3 is consistent with a redshift of $z = 6.604 \pm 0.002$, and thus implies a relatively small velocity offset from Lyα of $\sim$100 km s^{-1} or less, being closer in velocity to the systemic redshift of clumps A or B ($z = 6.601 \pm 0.001$; see Fig. 5), than to the slightly lower redshifts measured for the other components in the CR7 system ($z = 6.593$–6.600; M17). However, while the line is spatially offset from A and is closest to the UV clump B (see Fig. 1 for spatial context), it is not found to be co-located with B and thus may trace another component in the system. New observations are required to improve the flux constraints on HeII and to locate it spatially.

When we analyse OB1 and OB2 separately (see Fig. 5), or when we stack these without OB3 we find no significant evidence of the presence of HeII above 2.5σ. For the stack of OB1 and OB2, sampling a PA angle of 0°, we find an HeII flux upper limit (2.5σ) of $<4.1 \times 10^{-17}$ erg s^{-1}cm^{-2} (Table 1). However, stacking the three different OBs together leads to a detection of HeII at the $\approx3.3\,\sigma$ level in our analysis, with a flux of $2.0^{+0.6}_{-0.6} \times 10^{-17}$ erg s^{-1} cm^{-2}. The lower flux we find compared to S15 is due to the different flux calibration which in S15 was based on UltraVISTA *J* band. Finally, in Fig. 6, we show the results of our MC analysis for OB3 which contain the observations that dominate the HeII signal. We compare it to the results presented in S15 after correcting them for the wavelength offset (see e.g. Fig. A1 and Section 2.2), converting λ_{air} to λ_{vacuum} and scaling the counts to flux. We find a general good agreement within our errors, consistent with the signal being dominated by OB3. Note that in our analysis, we do not smooth the data or bin it beyond one-third of the resolution, unlike S15.

While we recover the HeII emission line and identify the signal as coming from OB3 we still measure a lower significance than reported in S15. This is mostly driven by the different methods used here, together with a new reduction. Furthermore, in order to place such reduced significance of an emission line at high redshift into context (see also Shibuya et al. 2018b), we investigate spectra of $z \sim$ 6–8 sources with published detections of high ionization UV lines in the literature. We find that in general lines are less statistically significant or, in some cases, consistent with not being detected above 2.5σ in our framework. For example, we recover results for COSz2 (Laporte et al. 2017b), there is partial agreement for COSY (Laporte et al. 2017b; Stark et al. 2017; Smit et al. 2018), but we fail to detect ($<2.5\,\sigma$) Lyα for A2744 (Laporte et al. 2017a). We present a more general comparison and discussion between our MC analysis and more widely used methods in the literature to measure the S/N of lines in Appendix E.

3.1.3 *Searching for other lines in X-SHOOTER*

We conduct an investigation of the full X-SHOOTER spectra, both on the full stack and also per OB. We search for UV rest-frame lines with FWHMs from 150 to 1500 km s^{-1} with redshifts from $z = 6.58$ to 6.606. In addition, we also follow the methodology of Sobral et al. (2018b). We do not detect any line above 2.5σ apart from Lyα and HeII. We nevertheless note that there could be a potential emission line below 2.5σ in OB3. We find it in the VIS arm (showing the negatives from offsetting along the slit; see Fig. 7) spatially coincident with Lyα. For $z = 6.60$, the potential emission line (S/N$\sim$2) is closest to the expected rest-frame wavelength of the NV doublet (see Fig. 7), but would imply a redshift of $z = 6.583 \pm 0.001$ for it to be 1238.8 Å (see e.g. Tilvi et al. 2016; Hu et al. 2017; Laporte et al. 2017b, for NV detections in other sources at $z \sim 7$).

3.1.4 *The nature of CR7 with SINFONI*

One can further investigate the presence and flux of HeII in CR7 by exploring SINFONI data. In Fig. 8, we show the 1D stacks. We show these for different extraction apertures. We assume the source is in the centre of the 3D stacked cube which should correspond to the peak of Lyα emission due to the blind offset applied, per OB (see Section 2.3). We visually search for potential emission in 2D by binning the data spectrally based on the HeII signal in X-SHOOTER's OB3, and find a potential signal from HeII in three of the OBs, with the strongest signal being found in the second OB, consistent with that found in S15 by using SINFONI data only. However, by measuring the noise on such wavelength slices (with apertures of $\sim$1 arcsec), we find that such signals on their own are of low significance ($<2\,\sigma$).

Our MC analysis on the 1D stacks reveals tentative detections of HeII at the $\approx2.5\sigma$ level for the 0.9 and 1.4 arcsec apertures (Fig. 8) used, yielding fluxes of $0.5^{+0.3}_{-0.2} \times 10^{-18}$ erg s^{-1} cm^{-2} and an FWHM of 160 ± 70 km s^{-1}. The line is found at a wavelength of $\lambda_{vacuum,\,obs} = 12475.3$ Å, matching very well the wavelength found with X-SHOOTER. If we use the 2.5σ as an upper limit for the HeII flux assuming a non-detection, we find $<1.3 \times 10^{-17}$ erg s^{-1} cm^{-2}.

[5]Splitting OB3 in different sets of exposures leads to very low S/N, but we do not find any single exposure that is dominating the signal. This means the signal is not a cosmic ray or an artefact. Nevertheless, given the low S/N from just one OB, there is still the chance that some significant OH variability during the observations could have at least contributed to boosting the signal, although the errors take OH lines into account.

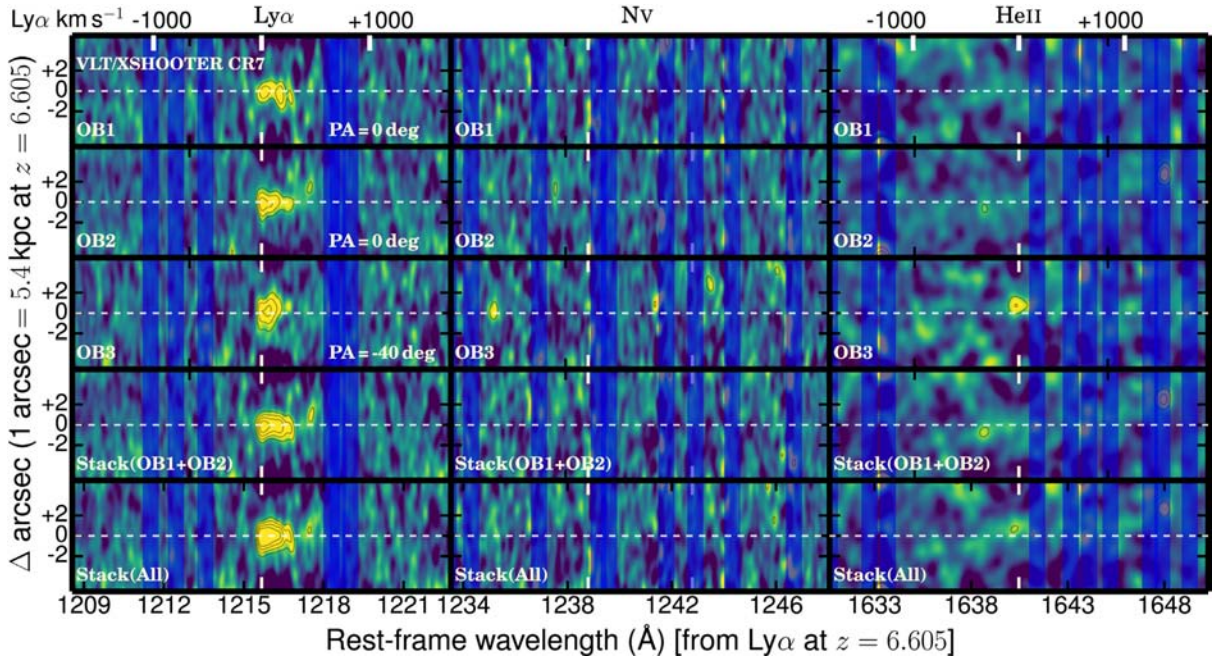

Figure 7. Our final reduced 2D X-SHOOTER spectra, zoomed-in at the expected positions of Lyα, NV, and HeII. We use a 3 spectral–spatial pixel Gaussian kernel to smooth the data and we show data in S/N space. Spatial contours show the 2σ, 3σ, 4σ, and 5σ levels and we use contrast cut-offs at -1σ and $+2\,\sigma$. The location of sky lines are also labelled. HeII is detected in OB3 at a $\approx 3\sigma$–4σ level (depending on the statistical method) with a spatial offset of +0.8 arcsec towards clump B. In OB3, we also find a tentative emission line blueshifted by ∼800–900 km s^{-1} to the expected wavelength of NV, but we find that this is $<2.5\sigma$ in our analysis and thus not significant with the current data.

This limit is consistent with the X-SHOOTER results, but favours a lower flux for HeII, much closer to $\sim 1 \times 10^{-17}$ erg s^{-1}cm^{-2}. This would imply an observed HeII/Lyα ratio of $\lesssim 0.06$. We find no other emission line in the SINFONI spectra for rest-frame wavelengths of ∼1450–1770 Å

3.2 Variability: UltraVISTA

We combine data from different epochs/DRs of UltraVISTA (McCracken et al. 2012; Laigle et al. 2016) to constrain the potential variability of CR7. Note that CR7 is found very close to the overlap between the deeper/shallower UltraVISTA observations, with a strong gradient of exposure time and therefore depth in the East–West direction. We start by studying magnitudes obtained with different apertures and for mag-auto, contained in the public catalogue, both for *Y* and *J*, tracking them from DR1 to DR2 and DR3. We find a large (in magnitude), $+0.51^{+0.14}_{-0.17}$ mag variation[6] in the *J*-band mag-auto magnitude of CR7 from the UltraVISTA public catalogues from DR2 to DR3 (see also Bowler et al. 2017b), while the magnitude stayed constant within the errors from DR1 to DR2 (see Appendix C).

In order to further investigate the potential variability of CR7 in the different DRs of UltraVISTA, we also conduct our own direct measurements on the data directly, fully available from the ESO archive. Furthermore, due to the potential problems with the usage of mag-auto, we use aperture photometry instead, placed over the UV clump A, at the centre of the CR7 system, and at the centre/peak of the Lyα emission: see Fig. 1. We measure AB magnitudes in apertures of 1.2, 2, and 3 arcsec for *Y*, *J*, *H*, and *K* and compare them with the measurements we obtain for DR2. For *H* and *K*, the errors are always very large (≈0.5 mag) to investigate variability. Full details of our measurements are provided in Appendix C.

Our results for aperture photometry on fixed positions for *Y* and *J* are presented in Fig. C3. We find no significant changes/variability for any of the locations, apertures or bands, as all differences are $<2\,\sigma$. Similarly to Bowler et al. (2017b), we find a change in the *J* magnitude of CR7 in 2 arcsec apertures of 0.21 ± 0.12 from DR2 to DR3 and in general there are weak trends of CR7 becoming fainter in fixed apertures from DR1 to DR3, but all these changes are at the $\sim 1\sigma$ level. We therefore conclude that there is no convincing evidence for strong variability (Δ mag >0.3) from the different DRs of UltraVISTA, but variability at the level of Δ mag ≈0.2 is consistent with the data.

3.3 *HST* grism observations: continuum results

The spectrum of CR7 is extracted for its multiple UV components A, B, and C detected with *HST* (see e.g. Fig. 1). We start by investigating the properties of the continuum and compare those with broad-band photometry. We measure $M_{\rm UV}$ (at rest frame ≈1500 Å) by integrating the flux between rest-frame 1450 and 1550 Å, and also by fitting a power law of the form λ^{β} between rest-frame 1450 and 2150 Å. All measurements are conducted per UV clump and by independently perturbing each spectral element within its Gaussian uncertainty and refitting 10 000 times. We present the median of all best fits, along with the 16th and 84th percentiles as the lower and upper errors in Table 2.

We find that our extraction of clump A yields $\beta = -2.5^{+0.6}_{-0.7}$ and $M_{\rm UV} = -21.87^{+0.25}_{-0.20}$. Our results are consistent with the photometric properties of the clump estimated as $\beta = -2.3 \pm 0.4$ and $M_{\rm UV} =$

[6]The magnitude difference is based on CR7 photometry, while errors are based on studying sources within 5 arcmin of CR7; this allows to derive a more robust error which is higher than the formal error in the catalogue.

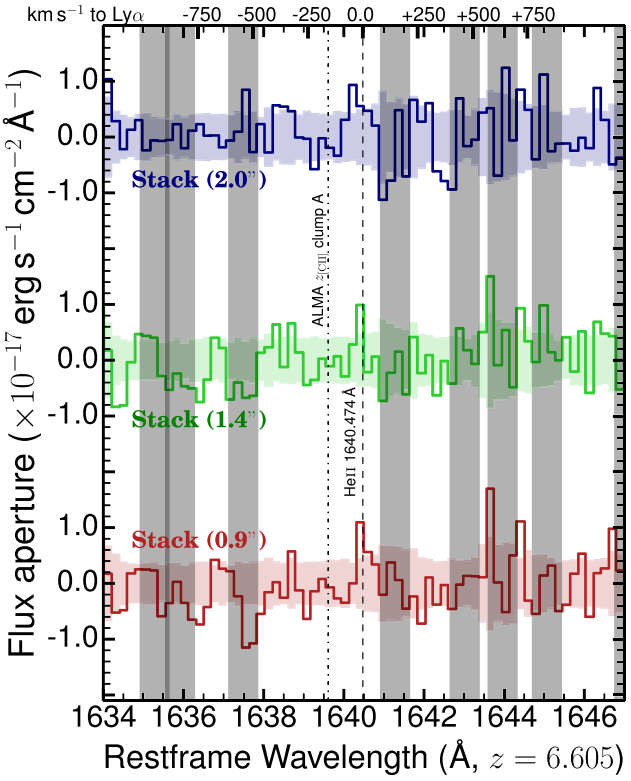

Figure 8. The extracted 1D SINFONI spectra at the expected location of HeII for stacks with different extraction apertures. The stacks show extractions obtained on the centre of the detector (assumed to trace the peak of Ly α) using the appropriate aperture corrections based on the standard stars available. We conservatively estimate the noise with randomly placed apertures per wavelength slice per extraction. Sky lines are clearly labelled. We find a tentative line consistent with the same wavelength ($\lambda_{\rm vacuum,\ obs}$ = 12475.3 Å) as found with X-SHOOTER, but implying a lower flux close to $\approx$0.5–1.0 $\times$ 10^{-17} erg s^{-1} cm^{-2}.

Table 2. The rest-frame UV properties of the three UV clumps in CR7 constrained with *HST*/WFC3 grism data. $M_{\rm UV,\ integral}$ is estimated from integrating the spectrum directly between rest-frame 1450 and 1550 Å. We provide the best power-law fits: β and the corresponding $M_{\rm UV,\ \beta}$ computed as the value of the best fit at $\lambda_0 = 1500$ Å. Values for each measurement are the median of all best fits and the upper and lower errors are the 16th and 84th percentiles.

Clump	$M_{\rm UV,\ integral}$	β	$M_{\rm UV,\ \beta}$
A	$-21.87^{+0.25}_{-0.20}$	$-2.5^{+0.6}_{-0.7}$	$-22.02^{+0.14}_{-0.13}$
B	$-21.0^{+0.5}_{-0.3}$	$-2.6^{+1.7}_{-1.7}$	$-20.9^{+0.4}_{-0.3}$
C	$-20.2^{+0.8}_{-0.4}$	–	–

-21.6 ± 0.1 (e.g. M17), although our measurement is completely independent of Ly α corrections which had to be applied in M17 as F110W is contaminated by Ly α (see also Bowler et al. 2017b). This shows we are able to recover the continuum properties of clump A, and that these continuum properties show no significant evidence for variability within the errors.

For the fainter clump B, we find much more uncertain values of β and $M_{\rm UV}$ (see Table 2), consistent within the errors with $\beta = -1.0 \pm 1.0$ and $M_{\rm UV} = -19.6 \pm 0.7$ from photometry (see e.g. M17). For clump C, we do not make any significant continuum detection and we can only constrain $M_{\rm UV}$ poorly.

3.4 *HST*/WFC3 imaging: is CR7 variable?

Our grism detection of continuum in B (albeit at low S/N) and non-detection of C is perhaps unexpected given that previous UV photometry implied clump C was slightly brighter than B (e.g. Bowler et al. 2017b). While our grism data are simply not constraining enough to investigate variability, new available imaging data taken in 2017 with WFC3 (program 14596, PI: Fan) with the same filters as in 2012 allow the opportunity to investigate variability in CR7 as a whole or in its individual components. The full details of our measurements are discussed in Appendix D.

We present our results, obtained with apertures (diameter) of 0.8, 0.4, and 0.4 arcsec placed on clumps A, B, and C in Table 3 and Fig. 9. We measure the full CR7 system, including any interclump UV light, with an aperture of 2 arcsec (see Table 3 for measurements with 1 arcsec apertures centred on each component); see Fig. 1. The errors are estimated by placing apertures with the same size in multiple empty regions around the source and taking the 16th and 84th percentiles. As Fig. 9 shows, there is no significant indication of variability for clumps A or B within the errors. The same is found for clump C in each individual band, although we find C to be brighter in 2017 by $\approx$0.2 mag in both F110W and F160W, with the combined change providing some tentative evidence for variability. As a full system, CR7 became brighter by 0.22 $\pm$ 0.10 mag, significant at just over $\approx 2\sigma$. This brightening seems to be caused in part by clump C, but in addition to flux in between the UV clumps. Further observations taken even more recently with *HST*/WFC3 program 14596 (PI: Fan; not publicly available yet) will be able to further clarify/confirm our results.

3.5 Grism observations: emission-line results

Fig. 10 presents the reduced *HST*/WFC3 2D spectra of each of the three clumps in CR7. For clump A, we show both the observed (continuum-dominated) spectrum, along with the continuum subtracted, while for clumps B and C we show the observed spectrum only. In Fig. 11, we present the extracted 1D spectra of each clump.

By using the best continuum fits shown in Fig. 11, we then continuum subtract the spectrum of each clump in order to look for any emission or absorption lines. We find no clear rest-frame UV emission or absorption line above a 3σ level in any of the three clumps. None the less, there are tentative signals which are above $\sim 2\sigma$: NIV] for the extraction of clump A ($z = 6.60 \pm 0.01$) and HeII for clump C (which would imply $z = 6.58 \pm 0.01$). Note that while NIV] (see also McGreer et al. 2018) for clump A is consistent with the systemic redshift now obtained for clump A with ALMA (M17), the potential HeII detection towards C would be consistent with a redshift of $z = 6.58$–6.59. This could be related with the blueshifted [CII] component found with ALMA towards C.

In order to better quantify the significance of all rest-frame UV lines, we measure all lines with GRIZLI[7]/EMCEE (MCMC), by fitting simultaneously to all of the exposure level 2D spectra, which is much more appropriate to grism data (see e.g. Kümmel et al. 2009; Brammer et al. 2012; Momcheva et al. 2016). We obtain the 2.5, 16, 50, 84, and 97.5 percentiles of the EMCEE chain, and show the results in Table 4. Our results show that there are no clear ($>3\sigma$) emission-line detections in either of the UV clumps. We also obtain very strong constraints on HeII centred on UV clumps A and B, showing no detections, with the 2σ limit for HeII flux in each of

[7] https://github.com/gbrammer/grizli/

Table 3. Results of our photometric study with *HST* data taken in 2012 and compared with more recent data taken with the same filters in 2017. We provide measurements centred on each clump and on the full system (see Fig. 1), both for apertures that capture each sub-component more optimally, but also with fixed 1 arcsec apertures. Errors are the 16th and 84th percentiles. We note that we do not apply corrections for the Ly α contribution to F110W. Δ F110W, Δ F160W, and $\Delta\beta_{\rm UV}$ are computed using F110W and F160W photometry and differences between 2017 and 2012 observations. For further details, see Appendix D.

Component	2012-03-02		2017-03-14		Δ: 2017–2012		
(Aperture, arcsec)	F110W	F160W	F110W	F160W	Δ F110W	Δ F160W	$\Delta\beta_{\rm UV}$
A (0.8)	$24.89^{+0.04}_{-0.04}$	$25.07^{+0.07}_{-0.07}$	$24.89^{+0.04}_{-0.04}$	$24.96^{+0.07}_{-0.07}$	$-0.01^{+0.06}_{-0.05}$	$-0.12^{+0.10}_{-0.10}$	$0.3^{+0.4}_{-0.4}$
B (0.4)	$27.04^{+0.15}_{-0.13}$	$26.70^{+0.17}_{-0.15}$	$26.99^{+0.13}_{-0.11}$	$27.04^{+0.27}_{-0.22}$	$-0.05^{+0.18}_{-0.19}$	$0.33^{+0.30}_{-0.29}$	$-1.2^{+1.1}_{-1.1}$
C (0.4)	$26.67^{+0.10}_{-0.09}$	$26.51^{+0.14}_{-0.13}$	$26.49^{+0.08}_{-0.08}$	$26.29^{+0.13}_{-0.11}$	$-0.18^{+0.12}_{-0.13}$	$-0.23^{+0.17}_{-0.17}$	$0.1^{+0.6}_{-0.7}$
CR7 (2.0)	$24.41^{+0.10}_{-0.08}$	$24.24^{+0.08}_{-0.07}$	$24.19^{+0.07}_{-0.05}$	$24.36^{+0.13}_{-0.12}$	$-0.22^{+0.10}_{-0.11}$	$0.12^{+0.15}_{-0.15}$	$-1.0^{+0.6}_{-0.6}$
CR7 (3.0)	$24.36^{+0.25}_{-0.17}$	$24.11^{+0.10}_{-0.09}$	$24.08^{+0.10}_{-0.07}$	$24.27^{+0.26}_{-0.20}$	$-0.28^{+0.19}_{-0.23}$	$0.16^{+0.25}_{-0.23}$	$-1.4^{+1.0}_{-1.1}$
A (1.0)	$24.82^{+0.05}_{-0.05}$	$24.97^{+0.08}_{-0.08}$	$24.78^{+0.05}_{-0.04}$	$24.91^{+0.09}_{-0.08}$	$-0.04^{+0.06}_{-0.06}$	$-0.06^{+0.11}_{-0.11}$	$0.1^{+0.4}_{-0.4}$
B (1.0)	$26.53^{+0.49}_{-0.35}$	$26.01^{+0.20}_{-0.18}$	$26.05^{+0.15}_{-0.13}$	$26.60^{+0.59}_{-0.41}$	$-0.48^{+0.42}_{-0.46}$	$0.58^{+0.59}_{-0.51}$	$-3.3^{+2.1}_{-2.2}$
C (1.0)	$26.38^{+0.35}_{-0.26}$	$25.80^{+0.16}_{-0.15}$	$25.97^{+0.14}_{-0.11}$	$25.79^{+0.21}_{-0.19}$	$-0.41^{+0.31}_{-0.34}$	$-0.02^{+0.25}_{-0.25}$	$-1.2^{+1.2}_{-1.3}$
CR7 (1.0)	$25.63^{+0.11}_{-0.11}$	$25.47^{+0.12}_{-0.11}$	$25.47^{+0.09}_{-0.08}$	$25.53^{+0.16}_{-0.15}$	$-0.17^{+0.14}_{-0.14}$	$0.06^{+0.20}_{-0.20}$	$-0.7^{+0.8}_{-0.8}$
CR7 (1.0)	$25.63^{+0.11}_{-0.11}$	$25.47^{+0.12}_{-0.11}$	$25.47^{+0.09}_{-0.08}$	$25.53^{+0.16}_{-0.15}$	$-0.17^{+0.13}_{-0.14}$	$0.06^{+0.20}_{-0.19}$	$-0.7^{+0.7}_{-0.7}$

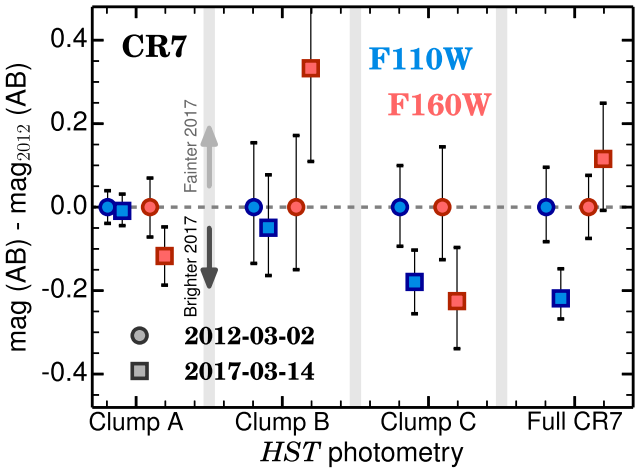

Figure 9. The difference in magnitudes for each UV clump in CR7, measured from *HST*/WFC3 photometry with the F110W and F160W filters in 2012 and in recent data taken in 2017. We find that while there is tentative evidence for clump C to have become brighter from 2012 to 2017 (when both bands are taken together), there is no convincing evidence for any of the clumps individually to have varied. However, the system as a whole is found to be brighter in the F110W filter by $-0.22^{+0.10}_{-0.11}$ mag. We find this to be due to both clump C and interclump light, particularly between clumps C and B.

those clumps being $<6 \times 10^{-18}$ erg s^{-1} cm^{-2}. This strongly implies that any HeII signal in X-SHOOTER is not coming directly from the UV components of either A or B, in agreement with the X-SHOOTER results, as otherwise it should have been detected at a $\sim 4\sigma$–5σ level. Interestingly, for clump C, there is a potential signal from HeII (see Table 4), as we find that 97.5 per cent of realizations result in an HeII flux of up to 17.1×10^{-18} erg s^{-1} cm^{-2}, with a central value of $(10 \pm 4) \times 10^{-18}$ erg s^{-1} cm^{-2}.

Furthermore, in order to conduct our full analysis self-consistently, we also apply our MC analysis in the same way as for X-SHOOTER and SINFONI (Sobral et al. 2018b) on the extracted 1D grism spectra per clump. We find that NIV] in clump A and HeII in clump C are significant at just above 2.5 σ, while all the other lines are $<2.5\,\sigma$. The full results, including the limits[8] for the lines that we do not detect above 2.5σ are provided in Table 5.

4 CLOUDY MODELLING AND THE PHYSICAL CONDITIONS OF CR7

Here, we explore the best constraints on a variety of lines (see Tables 5 and 6) to infer the possible physical properties of CR7, exploring its uniqueness as a $z \sim 7$ source for which we already have a wealth of resolved information despite the limited amount of telescope time invested.

In order to explore a relatively wide range of physical conditions that may be found in CR7, we use the CLOUDY (v 13.03) photoionization code (Ferland et al. 1998, 2013). Further details are given in Sobral et al. (2018b). Table B1 summarizes the key physical conditions. Briefly, we use three kinds of models (for a similar, more extensive analysis, see also, e.g. Nakajima et al. 2018): (i) power laws to mimic the spectra of AGN, (ii) stellar spectra from BPASS (Eldridge & Stanway 2009; Stanway, Eldridge & Becker 2016; Eldridge et al. 2017), and iii) blackbody models to further interpret and make simple predictions. We note that as a first step, and for simplicity, we only ionize the gas using photons. Shock ionization may in principle also play a role (e.g. Allen et al. 2008; Jaskot & Ravindranath 2016), which could be explored once observations provide detections in a range of lines, and particularly to explore spatially resolved emission-line ratio maps (see e.g. Miley & De Breuck 2008; Comerford et al. 2017; Morais et al. 2017).

4.1 The physical conditions in CR7 with current constraints: the full system

We use our simple CLOUDY grid predictions and the methodology presented in Sobral et al. (2018b) to interpret what the current measurements and constraints of several lines in CR7 imply. We start

[8]In order to estimate conservative 2.5σ limits in a self-consistent way we determine the -2.5σ and 2.5σ flux values (corresponding to 0.62 and 99.38 percentiles) and shift the mid-point between both to a flux of zero as we assume a non-detection. Our 2.5σ upper limit is then determined as the difference between 0σ and 2.5σ.

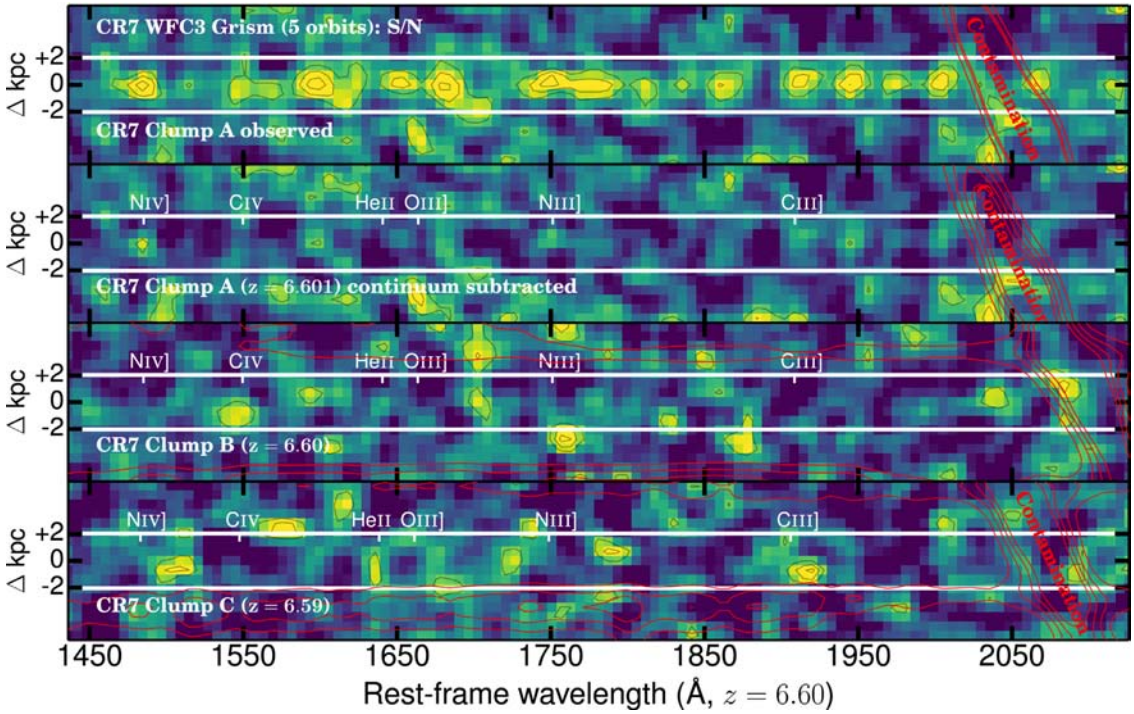

Figure 10. The final *HST*/WFC3 grism 2D reduced spectra, smoothed by 1 spatial–spectral pixel, for each of the three UV clumps in CR7: A, B, and C (see Fig. 1). All 2D here are shown in S/N space (contours: 2σ, 3σ, 4σ, and 5σ), with the noise estimated away from the location where each clump is found. We use contrast cut-offs of $-1\,\sigma$ and $+3\,\sigma$. For A, we show both the observed spectra (top) and the continuum subtracted 2D spectra. We show locations which were contaminated by nearby sources (contamination was subtracted but can still result in residuals). We also show the expected location of rest-frame UV lines using redshifts obtained with ALMA-[CII] (M17) close to the position of each clump and also an indicative 'slit' of 0.7 arcsec that would contain close to 100 per cent of the flux of each clump. We note that our 1D extraction is based on the 2D image of *HST* of each clump. Apart from detecting continuum, no clear emission line $>3\sigma$ is found for any of the three clumps.

by investigating the 'full' CR7 system as a whole using flux measurements from X-SHOOTER and SINFONI. We note that if one assumes that no line is detected apart from Ly α and only upper limits are used, models are, not surprisingly, completely unconstrained.

Due to the HeII flux constraints for the full system as a whole (implying a rest-frame EW of 26 ± 9 Å; see Tables 5 and 6), we find that standard BPASS models at 'normal' metallicities struggle to fully reproduce some of the observations, although, as Bowler et al. (2017b) showed, modified BPASS models with super-solar α elements at extremely low metallicity are able to reproduce the observations (see Bowler et al. 2017b). Furthermore, our simple power-law and blackbody models can both easily reproduce the observations, implying gas-phase metallicities of ≈10–20 per cent solar and ionization parameters of $\log U \approx -3$, but with large uncertainties of over 1 dex in all parameters using our very wide model grid.

4.2 CR7 resolved: the nature of each individual UV clump

For clump A, the tentative detection of NIV] (with an EW_0 of 24^{+11}_{-9} Å) and the non-detections of other lines, allow to place some constraints on the nature of the source, suggesting a high Nitrogen abundance and a high effective temperature, closer to $T_{\rm eff} \sim 100$ K. However, there is currently no strong evidence for the presence of an AGN, as stellar models (particularly at lower metallicities and/or with binaries) can reproduce the emission-line ratios within the large uncertainties. Nevertheless, the metallicity is consistent with ≈0.1–0.2 $Z_\odot$ as suggested by ALMA observations (based on the [CII]/UV ratio; M17).

Current flux and EW upper limits for clump B (Tables 5 and 6) do not allow to truly constrain the physical conditions that we explore, but we note that ALMA results hint for a metallicity of ≈0.1–0.2 $Z_\odot$. Our non-detection of any high ionization UV lines in clump B does not provide any evidence for an unusually high ionization parameter or for strong AGN activity (see also e.g. Nakajima et al. 2018), although some AGN activity is still possible. We further constrain the physical conditions using the UV + FIR SFR measured per clump (M17), not allowing models to significantly over or underestimate by factors of more than two the SFR per clump.

For clump C, the tentative detection of HeII at a very high EW (with EW_0 of 98^{+49}_{-43} Å) brings in some evidence of its potential AGN nature, while the non-detections of the other lines are also consistent with a potential low-metallicity AGN. By using all constraints, models suggest that C can be powered by an ionization source with roughly $\log U \approx -2$ and surrounded by a relatively low-metallicity gas (≈0.1–0.2 $Z_\odot$), but the constraints are currently very weak and deeper observations are required to improve the constraints; see e.g. Table 6 (see also Dors et al. 2018).

We conclude that with the current uncertainties, all three clumps are consistent with being relatively young starbursts with similar metal-poor gas-phase metallicities of ∼0.05–0.2 $Z_\odot$. There is currently no strong evidence for the presence of an AGN in either clumps A or B, and there is only tentative evidence for clump C to have a higher ionization parameter and to potentially host an AGN.

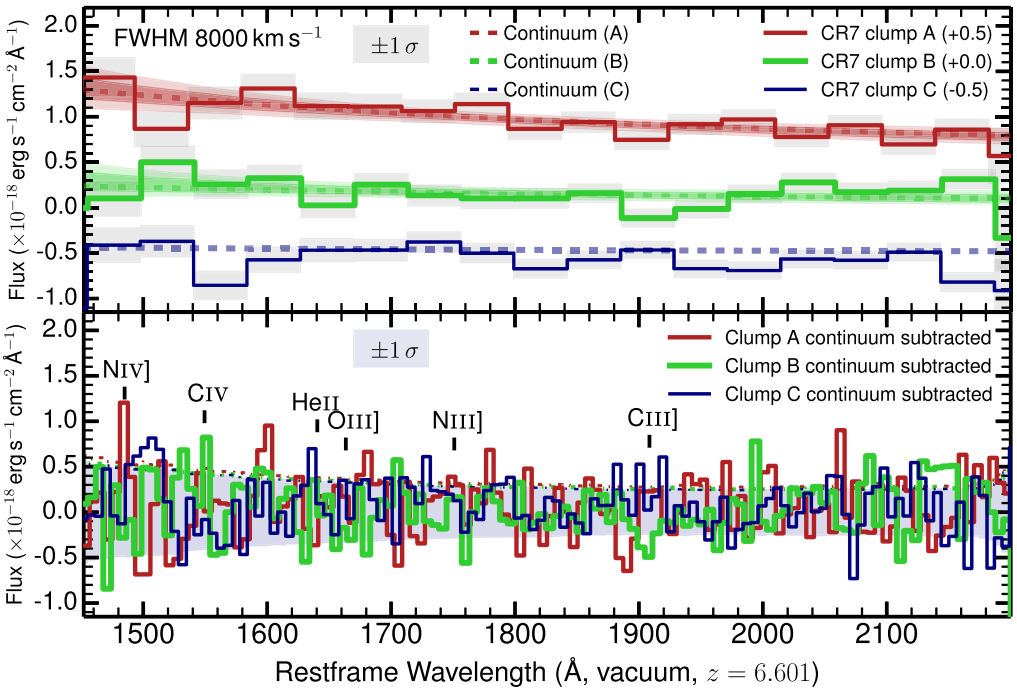

Figure 11. *HST*/WFC3 grism 1D spectra of the three UV clumps of CR7 extracted based on the UV detections of each clump in the pre- and post-images with the F140W filter. Top: clump A is significantly detected in the UV continuum and is well fitted with $\beta = -2.5^{+0.6}_{-0.7}$ and $M_{\rm UV} = -21.87^{+0.25}_{-0.20}$; we show the 16–84 and 2.3–97.7 percentile contours for all fits. Clump B is also detected in the rest-frame continuum but at a much lower significance, while clump C is not significantly detected in the continuum. Bottom: after continuum subtracting the spectra of each clump we find no significant detection above 3σ of any rest-frame UV line. There are only tentative detections of NIV] in clump A and HeII in clump C. The resolved spectra also show that any potential HeII emission from the UV clumps would have to likely come from or near clump C and not clump A. We assign relatively strong limits to all observed rest-frame UV lines, which we use to further interpret CR7.

Table 4. Results from the MCMC chain to constrain the line fluxes of each clump within CR7 for our *HST*/WFC3 grism data (A, B, and C) after subtracting the UV continuum per clump. We show the central value (best flux) and the percentiles, corresponding to $\pm1\,\sigma$ and $\pm2\,\sigma$. All fluxes are in 10^{-18} erg s^{-1} cm^{-2}. We find no significant detection above $3\,\sigma$ of any UV line within any of the clumps. However, we find potential detections of NIV] in clump A and HeII in clump C, both at over 2σ.

Emission	2.5 per cent	16 per cent	50 per cent	84 per cent	97.5 per cent
Clump A	-2σ	-1σ	central	$+1\sigma$	$+2\sigma$
NIV] 1485	0.21	7.66	14.78	20.94	26.69
CIV 1549.5	− 7.45	− 2.23	3.13	8.70	15.07
HeII 1640.5	− 13.60	− 8.70	− 3.66	1.48	5.46
OIII] 1663.5	− 6.36	− 2.27	2.33	7.11	11.22
NIII] 1751	− 2.54	1.26	5.11	9.00	13.37
CIII] 1908.5	− 5.45	− 2.36	1.22	4.76	7.49
Clump B					
NIV] 1485	− 16.04	− 11.06	− 5.16	0.67	6.50
CIV 1549.5	− 3.72	0.60	5.00	9.93	15.20
HeII 1640.5	− 10.28	− 6.35	− 2.07	1.87	5.99
OIII] 1663.5	− 14.24	− 10.49	− 6.08	− 2.11	2.22
NIII] 1751	− 9.27	− 5.67	− 2.04	1.42	4.33
CIII] 1908.5	− 15.26	− 12.33	− 9.18	− 6.14	− 3.02
Clump C					
NIV] 1485	− 7.29	− 1.88	4.52	10.06	15.44
CIV 1549.5	− 10.57	− 6.43	− 2.34	2.24	6.72
HeII 1640.5	1.83	5.70	9.60	13.66	17.12
OIII] 1663.5	− 8.08	− 3.87	0.23	4.45	8.01
NIII] 1751	− 4.19	− 0.92	2.42	5.58	8.62
CIII] 1908.5	− 1.93	0.98	4.01	7.09	9.83

Table 5. A summary of the high ionization rest-frame UV lines investigated for CR7 and/or their upper limits constrained in this work with our MC analysis. All fluxes are in units of 10^{-17} erg s^{-1} cm^{-2}. We list and use them in vacuum. We list fluxes for $\gtrsim 2.5\sigma$ detections, or the $<2.5\sigma$ upper limits constraints for the 'full system' (X-SHOOTER and SINFONI) and also for each of the clumps A, B, and C from the *HST*/WFC3 grism data.

Emission line λ_{vacuum} (Å)	Ionization energy (eV)	CR7 (Slit) X-SHOOTER	CR7 (0.9 arcsec) SINFONI	Clump A WFC3	Clump B WFC3	Clump C WFC3
Ly α 1215.67	13.6	17 ± 1^a	–	8.3 ± 0.7^a	2.7 ± 0.5^a	1.3 ± 0.4^a
NV 1238.8,1242.78	77.4	<1.4	–	–	–	–
OIV] 1401,1407	54.9	<3.0	–	–	–	–
NIV] 1483.4,1486.6	47.4	<2.2	<5.1	$1.9^{+0.7}_{-0.7}$	<2.6	<2.8
CIV 1548.2,1550.77	47.9	<1.5	<1.0	<2.3	<2.2	<2.1
HeII 1640.47	54.4	$2.0^{+0.6}_{-0.6}$	$0.5^{+0.3}_{-0.2}$	<2.7	<1.9	$1.1^{+0.5}_{-0.4}$
OIII] 1661,1666	35.1	<2.6	<2.6	<2.3	<1.8	<1.8
NIII] 1749.7,1752.2	29.6	<15.9	<30.7	<1.6	<1.5	<1.7
CIII] 1907,1910	24.4	<1.7	–	<1.5	<1.3	<1.4

(a): Ly α flux from the X-SHOOTER slit (observed) implies $5.9 \pm 0.5 \times 10^{-17}$ erg s^{-1} cm^{-2} (integration without Gaussian fitting). Ly α is clearly extended (S15), and thus the full slit losses are larger than for a simple point source; the full Ly α flux over the full CR7 system is estimated as $(17 \pm 1) \times 10^{-17}$ erg s^{-1} cm^{-2} (see Matthee et al. 2017a). We follow M17 and associate Ly α observed fluxes to clumps A, B, and C based on the 2D Ly α distribution from NB91 photometry. Note that these Ly α fluxes have not been measured directly with spectroscopy, and are thus very uncertain.

Table 6. Rest-frame EW_0 constraints for UV lines (see Table 5) inferred from our WFC3 grism observations of each of the three UV clumps of CR7. As a comparison, we also provide equivalent measurements for the 'full' CR7 system based on our X-SHOOTER flux constraints. We use the flux limits provided in Table 5 and [M_{UV}, β] of [-22.2 ± 0.1, -2.2 ± 0.4], [-22.0 ± 0.2, -2.5 ± 0.7], [-20.9 ± 0.4, -2.6 ± 1.7], and [-20.1 ± 0.3, -2.3 ± 0.8] for the full system, clumps A, B, and C, respectively, in order to predict the continuum at the rest-frame wavelength of each emission line. We list fluxes accompanied by the 16 and 84 percentiles if a line is significant at $\gtrsim 2.5\sigma$ or we list the $<2.5\sigma$ non-detections constraints.

Emission line	CR7 (Å)	Clump A (Å)	Clump B (Å)	Clump C (Å)
Ly α	122^{+16}_{-15}	65^{+16}_{-12}	57^{+45}_{-24}	63^{+28}_{-26}
NV	<11	–	–	–
NIV]	<24	24^{+11}_{-9}	<96	<214
CIV	<18	<34	<88	<180
HeII	26^{+9}_{-9}	<45	<88	98^{+49}_{-43}
OIII]	<37	<39	<85	<182
NIII]	<253	<32	<85	<195
CIII]	<32	<37	<95	<189

5 DISCUSSION

CR7 has previously been discussed as being powered by very low-metallicity stars (PopIII-like; Sobral et al. 2015; Visbal et al. 2016), as a candidate for being a DCBH (e.g. Pallottini et al. 2015; Sobral et al. 2015; Agarwal et al. 2016, 2017; Hartwig et al. 2016), or as hosting a significant population of young, binary and/or Wolf-Rayet stars at extremely low metallicities (e.g. Bowler et al. 2017b). The observed Ly α and HeII EWs based on UltraVISTA DR2 public photometry in S15 could only be explained by an extreme hard ionizing spectrum, implying a high effective temperature and an extremely low metallicity of $\approx$0.05–0.5 per cent solar (Hartwig et al. 2016; Bowler et al. 2017b). Different components of CR7 have now been spectroscopically confirmed to be part of the same system (M17), with velocity offsets of only a few hundred km s^{-1} at most, and with evidence of dynamics/potential merging activity (see Fig. 12). New observations of CR7 reveal the unique potential of bright enough targets at high redshift, allowing the first spatially resolved studies of both rest-frame UV lines and [CII] detections with ALMA (M17); see also Carniani et al. (2018a).

Overall, and specifically for clump A, our results show that the HeII/Ly α ratio is significantly lower than measured using UltraVISTA flux estimate of HeII (S15), with this ratio being more likely below $\sim$0.06 instead of close to $\sim$0.2 (see Sections 3.1.2 and 3.1.4). This rules out the most extreme DCBH scenarios for clump A. Together with the [CII] detection in A (M17), our results imply a metallicity of roughly 0.1–0.2 $Z_\odot$ for clump A (to be confirmed/verified with *JWST*), thus becoming globally inconsistent with a 'PopIII-like' scenario metallicity ($\sim$0.005 $Z_\odot$; Bowler et al. 2017b). Our latest results indicate that A is a more 'normal' starburst, consistent with feedback processes already fully in place, as indicated from the Ly α line profile modelling (Dijkstra et al. 2016). It is interesting that while ALMA provides a detection of Carbon (M17) in CR7's clump A (also in/around clumps B and C; see Fig. 12), and even though we estimate a metallicity of roughly 0.1–0.2 $Z_\odot$ (similar to sources studied by e.g. Stark et al. 2015b), we do not detect any high ionization Carbon line (e.g. CIV or CIII]), down to rest-frame EW upper limits of $\approx$37, 34 Å in CIII] and CIV, respectively. This is consistent with the hypothesis explored in Matthee et al. (2017a) that current CIV and CIII] detections in galaxies at the epoch of reionization are only possible for even intrinsically brighter sources with much higher SFRs (UV brighter or with significant lensing amplifications) and/or AGN (e.g. Laporte et al. 2017b; Shibuya et al. 2018b; Sobral et al. 2018b).

Current observational constraints point towards CR7's clump C (e.g. Dors et al. 2018) or additional interclump components (Fig. 12) as the most puzzling and uncertain at the moment. This component seems to show the largest blueshift and presents evidence for the presence of a high EW HeII line (see Table 6). Furthermore, HeII is also tentatively detected between clumps B and C. While there are indications that C may host an AGN/high ionization UV source, this would be somewhat puzzling in other regards as it would imply a likely low black hole mass given its sub-L$*$ luminosity in both observed Ly α and in the UV (in our grism observations, it is the faintest component in CR7). Some obscuration could in principle be invoked to explain the low luminosity in Ly α and the UV for clump C, but ALMA observations (M17) do not detect any dust. However, current ALMA observations are not sensitive to significantly hot dust that may be present in C.

In principle, future X-ray observations may also help to determine the nature of these high-redshift sources, but these may have to

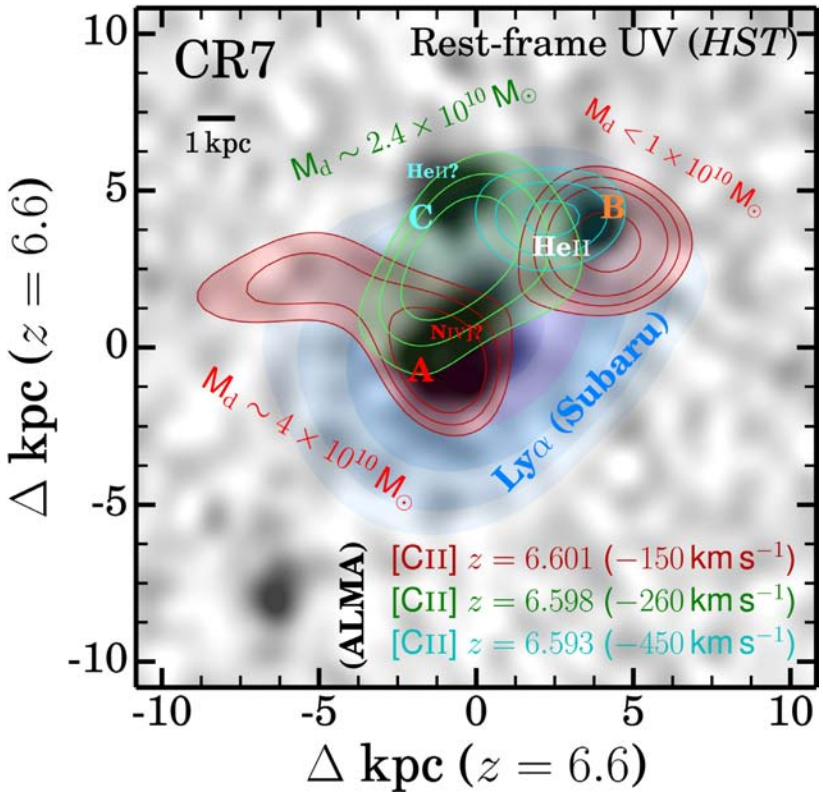

Figure 12. A summary of the results presented or discussed in this paper on CR7, resulting from observations obtained with *Subaru*/S-Cam (S15), *HST*/WFC3 (S15, and this study), ALMA (M17), and the VLT (this study). We show how the Ly α halo extends over the three rest-frame UV clumps, peaking closer to the brightest clump A. [CII] follow-up with ALMA reveals at least four different components, with the brightest and likely most massive being coincident with clump A but extending beyond it. There is a blueshifted component closest to clump C (but not coincident with it) which is potentially massive and close to the inferred location of HeII found with X-SHOOTER in OB3 (labelled in white; see Fig. 1). We also indicate the tentative emission lines found in clumps A and C, but we note that those are $<3\sigma$.

achieve significantly high resolution (if they are to locate AGN within multicomponent galaxies) and be relatively deep to detect the presence of an AGN in e.g. clump C. Given its luminosity in the UV and also its potential HeII luminosities, one would expect X-ray luminosities of $\approx 10^{42}$ erg s^{-1}, about $\sim$4 times lower than predicted by Pallottini et al. (2015) due to the much lower HeII luminosity in clump C than originally estimated using UltraVISTA photometry (S15). Therefore, identifying AGN will likely be much more efficient with *JWST*, particularly with the integral field unit (IFU) on NIRSpec, at least until the launch of the *Athena* X-ray mission.

Our results also point towards potential consequences when interpreting emission lines from clump C and from other clumps/the full system. Given the geometry of the system and the small velocity offsets between components (see M17, and Fig. 12), it is possible that each clump is differentially illuminated by a time-dependent AGN + SF composite SED. Observations with *JWST* obtained over $\sim$1–2 yr could be crucial to test how important any time variability and the illumination from different clumps may be. This would be important to e.g. understand whether illumination from another clump (e.g. C) could give rise/be responsible for potential high ionization lines seen in the gas of another. Until then, detailed 3D simulations could be performed with full radiation transfer in order to further investigate similar systems (e.g. Carniani et al. 2018a; Matthee et al. 2018) and allow to make specific predictions, not only for CR7, but for other similar sources within the epoch of re-ionization, prior to the launch of *JWST* in a few years.

6 CONCLUSIONS

We presented new *HST*/WFC3 grism and imagining observations and combined those with a re-analysis of flux-calibrated X-SHOOTER and SINFONI data obtained with the VLT for the most luminous Ly α emitter at $z = 6.6$, CR7 (S15). We investigated the continuum, variability and rest-frame UV lines of the source as a whole and its three UV components. We find that:

(i) The Ly α profile of CR7 is broader in the East–West direction (FWHM $= 300^{+56}_{-40}$ km s^{-1}) compared to a PA angle of -40° that matches the major axis of Ly α emission (FWHM $= 180^{+50}_{-30}$ km s^{-1}) and that connects clumps A and B. The stack of all OBs yields an Ly α FWHM $= 270^{+35}_{-30}$ km s^{-1}, in good agreement with S15.

(ii) Our re-reduced, flux-calibrated X-SHOOTER stacked spectrum of CR7 reveals a $\approx 3\sigma$ HeII detection in CR7 with a flux of $2.0^{+0.6}_{-0.6} \times 10^{-17}$ erg s^{-1} cm^{-2}. Such signal is found to be dominated by OB3 which on its own yields a flux of $3.4^{+1.0}_{-0.9} \times 10^{-17}$ erg s^{-1} cm^{-2}.

(iii) The HeII line detected in OB3 is spatially offset by $+0.8$ arcsec from clump A towards B but does not coincide with the UV clump B. The stack of OB1 and OB2 result in a non-detection ($<2.5\sigma$) of HeII. *HST* grism data confirm that there is no strong HeII emission directly on UV clumps A or B. Our re-reduced

SINFONI data present some evidence for HeII but suggests a flux closer to $\approx 1 \times 10^{-17}$ erg s^{-1} cm^{-2}, with our MC method yielding $0.5^{+0.3}_{-0.2} \times 10^{-17}$ erg s^{-1} cm^{-2}.

(iv) No statistically significant changes are seen in *Y* photometry from DR2 to DR3, but we find a change of $+0.51^{+0.14}_{-0.17}$ mag (mag-auto) in the UltraVISTA *J*-band public catalogue for CR7 as a whole from DR2 to DR3. However, we find no statistically significant variation ($<2\,\sigma$) when we conduct aperture photometry with carefully estimated errors.

(v) Our WFC3 grism spectra provide a significant detection of the UV continuum of CR7's clump A, yielding an excellent fit to a power law with $\beta = -2.5^{+0.6}_{-0.7}$ and $M_{\rm UV} = -21.87^{+0.25}_{-0.20}$. This is fully consistent with the broad-band photometry and with no variability for clump A.

(vi) Careful measurements of F110W and F160W data of CR7 taken in 2012 and 2017 reveal no significant variability in either bands for clumps A or B, but there is a tentative combined brightening of clump C. CR7 as a whole (aperture of 2 arcsec encompassing the three clumps) changes by $-0.22^{+0.10}_{-0.11}$ in F110W, providing 2.2σ evidence for variability. We find that this change can be explained by both clump C and also interclump light, but requires confirmation. No variability is seen in F110W in A (within ± 0.05 mag) or B (within ± 0.2 mag).

(vii) *HST* grism data do not detect any rest-frame UV line in any of the UV clumps above $3\,\sigma$, with rest-frame EW$_0$ limits varying from <30 Å to <200 Å. We find a tentative ($\approx 2.5\,\sigma$) HeII line in clump C's data, yielding a flux of $1.10^{+0.50}_{-0.46} \times 10^{-17}$ erg s^{-1} cm^{-2} and $z = 6.574^{+0.019}_{-0.013}$.

(viii) Our results show that the HeII/Ly α ratio for clump A is significantly lower than measured using the UltraVISTA flux estimate of HeII (S15), with this ratio being likely closer to $\lesssim 0.06$ instead of close to ~ 0.2. This rules out the most extreme DCBH scenarios for clump A.

(ix) We perform CLOUDY modelling and obtain limits on the metallicity and constrain the ionizing nature of CR7. We conclude that CR7 is likely actively forming stars without any clear AGN activity in clumps A and B, with a metallicity of $\sim$0.1–0.2 Z$_\odot$ (to be confirmed/verified with *JWST*) and with component A experiencing the most massive starburst. Together with the [CII] detection in clumps A and B (M17), our results are globally inconsistent with a 'PopIII-like' scenario metallicity (~ 0.005 Z$_\odot$; Bowler et al. 2017b) for clumps A and B.

(x) Component C, or an interclump component, may host a high ionization source/AGN and could be variable, although the evidence for variability is only at the $\approx 2.2\sigma$ level and requires further, deeper observations with *HST* to be confirmed.

Overall, our results reveal that CR7 is a complex system (see Fig. 12) which may be giving us an early glimpse of the complicated rapid assembly processes taking place in the early Universe. The high-resolution observations presented here, those obtained with ALMA (e.g. Jones et al. 2017a; Matthee et al. 2017b; Carniani et al. 2018a) and recent simulations for galaxies at $z \sim 7$ (e.g. Pallottini et al. 2017; Behrens et al. 2018; Gallerani et al. 2018) point towards early galaxies being chaotic collections of metal-poor merging clumps which will also likely bring along black holes and potentially lead to measurable variability. Such complex systems imply that the approach of simply placing a very narrow slit in a single UV light peak may only reveal part of the full picture, particularly if there is significant ionizing flux from nearby sources. It seems that the systems studied so far at $z \sim 7$–8 require spatially resolved observations, ideally obtained by IFU spectrographs, in order to identify the nature of different components (e.g. Carniani et al. 2017, 2018a; Hashimoto et al. 2018). The current results also reveal the importance of simulations to take into account such complex systems by performing a full 3D radiation transfer for systems like CR7 and comparing with observations, particularly to constrain the role of multiple ionizing sources. Until *JWST* is launched, further spatially resolved observations of other bright enough systems which have been spectroscopically confirmed (e.g. Ouchi et al. 2013; Sobral et al. 2015; Hu et al. 2016; Matthee et al. 2017a, 2018; Carniani et al. 2018b) with MUSE, ALMA, and *HST* will assure an even more efficient and diverse laboratory to advance our knowledge of the early assembly of galaxies within the epoch of re-ionization. These can then be further applied to fainter and more numerous sources.

ACKNOWLEDGEMENTS

We thank the anonymous reviewer for the numerous detailed comments that led us to greatly improve the quality, extent, and statistical robustness of this work. DS acknowledges financial support from the Netherlands Organisation for Scientific research through a Veni fellowship. JM acknowledges the support of a Huygens PhD fellowship from Leiden University. AF acknowledges support from the ERC Advanced Grant INTERSTELLAR H2020/740120. BD acknowledges financial support from NASA through the Astrophysics Data Analysis Program, grant number NNX12AE20G and the National Science Foundation, grant number 1716907. We are thankful for several discussions and constructive comments from Johannes Zabl, Eros Vanzella, Bo Milvang-Jensen, Henry McCracken, Max Gronke, Mark Dijkstra, Richard Ellis, and Nicolas Laporte. We also thank Umar Burhanudin and Izzy Garland for taking part in the XGAL internship in Lancaster and for exploring the *HST* grism data independently.

Based on observations obtained with *HST*/WFC3 programs 12578, 14495, and 14596. Based on observations of the National Japanese Observatory with the Suprime-Cam on the *Subaru* telescope (S14A-086) on the big island of Hawaii. This work is based in part on data products produced at TERAPIX available at the Canadian Astronomy Data Centre as part of the Canada–France–Hawaii Telescope Legacy Survey, a collaborative project of NRC and CNRS. Based on data products from observations made with ESO Telescopes at the La Silla Paranal Observatory under ESO programme IDs 294.A-5018, 294.A-5039, 092.A-0786, 093.A-0561, 097.A-0043, 097.A-0943, 098.A-0819, 298.A-5012, and 179.A-2005, and on data products produced by TERAPIX and the Cambridge Astronomy Survey Unit on behalf of the UltraVISTA consortium. The authors acknowledge the award of service time (SW2014b20) on the William Herschel Telescope (WHT). WHT and its service programme are operated on the island of La Palma by the Isaac Newton Group in the Spanish Observatorio del Roque de los Muchachos of the Instituto de Astrofisica de Canarias. This research was supported by the Munich Institute for Astro- and Particle Physics of the DFG cluster of excellence 'Origin and Structure of the Universe'.

We have benefitted immensely from the public available programming language PYTHON, including NUMPY and SCIPY (Jones et al. 2001; Van Der Walt, Colbert & Varoquaux 2011), MATPLOTLIB (Hunter 2007), ASTROPY (Astropy Collaboration et al. 2013), and the TOPCAT analysis program (Taylor 2013). This research has made use of the VizieR catalogue access tool, CDS, Strasbourg, France.

All data used for this paper are publicly available, and we make all reduced data available with the refereed paper.

REFERENCES

Agarwal B., Johnson J. L., Zackrisson E., Labbe I., van den Bosch F. C., Natarajan P., Khochfar S., 2016, MNRAS, 460, 4003
Agarwal B., Johnson J. L., Khochfar S., Pellegrini E., Rydberg C.-E., Klessen R. S., Oesch P., 2017, MNRAS, 469, 231
Allen M. G., Groves B. A., Dopita M. A., Sutherland R. S., Kewley L. J., 2008, ApJS, 178, 20
Astropy Collaboration et al., 2013, A&A, 558, A33
Behrens C., Pallottini A., Ferrara A., Gallerani S., Vallini L., 2018, MNRAS, 477, 552
Bertin E., Arnouts S., 1996, A&AS, 117, 393
Bouwens R. J. et al., 2014, ApJ, 793, 115
Bouwens R. J., Illingworth G. D., Oesch P. A., Trenti M., Labbé I., Bradley L. et al., 2015, ApJ, 803, 34
Bowler R. A. A. et al., 2012, MNRAS, 426, 2772
Bowler R. A. A. et al., 2014, MNRAS, 440, 2810
Bowler R. A. A. et al., 2017a, MNRAS, 466, 3612
Bowler R. A. A., McLure R. J., Dunlop J. S., McLeod D. J., Stanway E. R., Eldridge J. J., Jarvis M. J., 2017b, MNRAS, 469, 448
Brammer G., Pirzkal N., McCullough P., MacKenty J., 2014, Technical Report, Time-varying Excess Earth-glow Backgrounds in the WFC3/IR Channel. Instrument Science Report WFC3 2014-03
Brammer G. B. et al., 2012, ApJS, 200, 13
Capak P. L. et al., 2015, Nature, 522, 455
Carniani S. et al., 2017, A&A, 605, A42
Carniani S. et al., 2018a, MNRAS, 478, 1170
Carniani S., Maiolino R., Smit R., Amorín R., 2018b, ApJ, 854, L7
Comerford J. M., Barrows R. S., Müller-Sánchez F., Nevin R., Greene J. E., Pooley D., Stern D., Harrison F. A., 2017, ApJ, 849, 102
de Barros S., Schaerer D., Stark D. P., 2014, A&A, 563, A81
Dijkstra M., Gronke M., Sobral D., 2016, ApJ, 823, 74
Dors O. L., Agarwal B., Hägele G. F., Cardaci M. V., Rydberg C.-E., Riffel R. A., Oliveira A. S., Krabbe A. C., 2018, MNRAS, 479, 2294
Dunlop J. S., McLure R. J., Robertson B. E., Ellis R. S., Stark D. P., Cirasuolo M., de Ravel L., 2012, MNRAS, 420, 901
Eldridge J. J., Stanway E. R., 2009, MNRAS, 400, 1019
Eldridge J. J. et al., 2017, PASA, 34, e058
Ferland G. J., Korista K. T., Verner D. A., Ferguson J. W., Kingdon J. B., Verner E. M., 1998, PASP, 110, 761
Ferland G. J. et al., 2013, RMAA, 49, 137
Gallerani S., Pallottini A., Feruglio C., Ferrara A., Maiolino R., Vallini L., Riechers D. A., 2018, MNRAS, 473, 1909
Gronke M., 2017, A&A, 608, A139
Harikane Y. et al., 2018a, PASJ, 70, S11
Harikane Y. et al., 2018b, ApJ, 859, 84
Hartwig T. et al., 2016, MNRAS, 462, 2184
Hashimoto T. et al., 2018, preprint (arXiv:1806.00486)
Hu W. et al., 2017, ApJ, 845, L16
Hunter J. D., 2007, Comput. Sci. Eng., 9, 90
Hu E. M., Cowie L. L., Songaila A., Barger A. J., Rosenwasser B., Wold I. G. B., 2016, ApJ, 825, L7
Jaskot A. E., Ravindranath S., 2016, ApJ, 833, 136
Jiang L. et al., 2017, ApJ, 846, 134
Jones E. et al., 2001, SciPy: Open Source Scientific Tools for Python. Available at: http://www.scipy.org/
Jones G. C., Willott C. J., Carilli C. L., Ferrara A., Wang R., Wagg J., 2017a, ApJ, 845, 175
Jones G. C. et al., 2017b, ApJ, 850, 180
Karman W. et al., 2017, A&A, 599, A28
Kümmel M., Walsh J. R., Pirzkal N., Kuntschner H., Pasquali A., 2009, PASP, 121, 59
Kuntschner H., Bushouse H., Kümmel M., Walsh J. R., MacKenty J., 2010, Proc. SPIE, 7731, 77313A
Laigle C. et al., 2016, ApJS, 224, 24
Laporte N. et al., 2017a, ApJ, 837, L21
Laporte N., Nakajima K., Ellis R. S., Zitrin A., Stark D. P., Mainali R., Roberts-Borsani G., 2017b, ApJ, 851, 40
Maiolino R. et al., 2015, MNRAS, 452, 54
Matthee J., Sobral D., Santos S., Röttgering H., Darvish B., Mobasher B., 2015, MNRAS, 451, 400
Matthee J., Sobral D., Darvish B., Santos S., Mobasher B., Paulino-Afonso A., Röttgering H., Alegre L., 2017a, MNRAS, 472, 772
Matthee J. et al., 2017b, ApJ, 851, 145
Matthee J., Sobral D., Gronke M., Paulino-Afonso A., Stefanon M., Röttgering H., 2018, preprint (arXiv:1805.11621)
McCracken H. J. et al., 2012, A&A, 544, A156
McGreer I. D. et al., 2018, MNRAS, 479, 435
Miley G., De Breuck C., 2008, A&AR, 15, 67
Modigliani A. et al., 2010, Proc. SPIE, 7737, 773728
Momcheva I. G. et al., 2016, ApJS, 225, 27
Morais S. G. et al., 2017, MNRAS, 465, 2698
Nakajima K. et al., 2018, A&A, 612, A94
Oke J. B., Gunn J. E., 1983, ApJ, 266, 713
Ota K. et al., 2014, ApJ, 792, 34
Ouchi M. et al., 2013, ApJ, 778, 102
Pacucci F., Pallottini A., Ferrara A., Gallerani S., 2017, MNRAS, 468, L77
Pallottini A. et al., 2015, MNRAS, 453, 2465
Pallottini A., Ferrara A., Gallerani S., Vallini L., Maiolino R., Salvadori S., 2017, MNRAS, 465, 2540
Popping G., Puglisi A., Norman C. A., 2017, MNRAS, 472, 2315
Raiter A., Fosbury R. A. E., Teimoorinia H., 2010, A&A, 510, A109
Salpeter E. E., 1955, ApJ, 121, 161
Santos S., Sobral D., Matthee J., 2016, MNRAS, 463, 1678
Schaerer D., Boone F., Zamojski M., Staguhn J., Dessauges-Zavadsky M., Finkelstein S., Combes F., 2015, AAP, 574, A19
Shibuya T. et al., 2018a, PASJ, 70, S14
Shibuya T. et al., 2018b, PASJ, 70, S15
Smit R. et al., 2018, Nature, 553, 178
Smith A., Bromm V., Loeb A., 2016, MNRAS, 460, 3143
Sobral D., Matthee J., Darvish B., Schaerer D., Mobasher B., Röttgering H. J. A., Santos S., Hemmati S., 2015, ApJ, 808, 139
Sobral D., Santos S., Matthee J., Paulino-Afonso A., Ribeiro B., Calhau J., Khostovan A. A., 2018a, MNRAS, 476, 4725
Sobral D. et al., 2018b, MNRAS, 477, 2817
Stanway E. R., Eldridge J. J., Becker G. D., 2016, MNRAS, 456, 485
Stark D. P. et al., 2015a, MNRAS, 450, 1846
Stark D. P. et al., 2015b, MNRAS, 454, 1393
Stark D. P. et al., 2017, MNRAS, 464, 469
Taylor M., 2013, Starlink User Note, 253
Tilvi V. et al., 2016, ApJ, 827, L14
Van Der Walt S., Colbert S. C., Varoquaux G., 2011, Comput. Sci. Eng., 13, 22
Venemans B. P. et al., 2012, ApJ, 751, L25
Visbal E., Haiman Z., Bryan G. L., 2016, MNRAS, 460, L59
Visbal E., Bryan G. L., Haiman Z., 2017, MNRAS, 469, 1456
Watson D., Christensen L., Knudsen K. K., Richard J., Gallazzi A., Michałowski M. J., 2015, Nature, 519, 327
Wilkins S. M., Bouwens R. J., Oesch P. A., Labbé I., Sargent M., Caruana J., Wardlow J., Clay S., 2016, MNRAS, 455, 659
Zabl J., Nørgaard-Nielsen H. U., Fynbo J. P. U., Laursen P., Ouchi M., Kjærgaard P., 2015, MNRAS, 451, 2050
Zheng Z.-Y. et al., 2017, ApJ, 842, L22

SUPPORTING INFORMATION

Supplementary data are available at *MNRAS* online.

Supplementary_Material_1.zip

Please note: Oxford University Press is not responsible for the content or functionality of any supporting materials supplied by the authors. Any queries (other than missing material) should be directed to the corresponding author for the article.

APPENDIX A: REDUCED DATA: PUBLIC RELEASE

We publicly release all spectroscopic and imaging data described and analysed in this paper. This includes the 2Ds from X-SHOOTER and *HST*/WFC3. We also release our extracted 1D spectra, flux calibrated, including our best estimate of the 1σ noise per wavelength element. We release these as fits files, available to download with the refereed paper. Raw data are also publicly available for all the data sets described here by querying the appropriate archives and proposal IDs.

A1 Comparison with S15: the NIR wavelength calibration offset

In Fig. A1, we show the offset between the wavelength calibration in the NIR from S15 and our reduction, resulting from the use of old arcs in S15; applying an offset of $\approx$+6.9 Å to the 1D of S15 is able to correct the wavelengths in the range covering HeII; see Section 2.2.

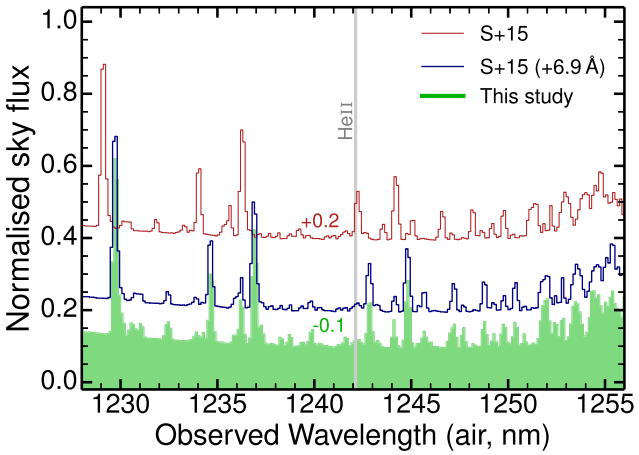

Figure A1. The arbitrarily normalized sky spectrum for the stack of the three OBs in the NIR arm around the observed emission line identified as HeII for CR7 for our reduction and a comparison to S15, showing an offset in the wavelength calibration. Applying an offset of +6.9 Å to the NIR spectrum presented in S15 results in a good agreement with our results. Note that we have shifted the normalized sky spectra in the *Y*-direction as indicated for clarity.

APPENDIX B: CLOUDY MODELLING

We present the main parameters explored in our CLOUDY modelling in Table B1, and also release all the models/CLOUDY grids in FITS format together with this paper. For more details, see Sobral et al. (2018b).

Table B1. Parameters and ranges used for the photoionization CLOUDY (Ferland et al. 1998, 2013) modelling presented in Sobral et al. (2018b) and used in this study. We vary density, metallicity, and the ionization parameter (log U) for star-like ionization, here modelled with BPASS (Eldridge & Stanway 2009; Stanway et al. 2016), or more simply with blackbodies of varying temperature from 20 to 160 K. AGN-like ionization is modelled using power-law sources with varying slopes.

Parameter	Range used for all models
Density (n_H cm^{-3})	30, 100, 300, 1000
Metallicity (log $Z_\odot$)	-2 to $+0.5$ (steps of 0.05)
Ionization parameter (log U)	-5 to $+2$ (steps of 0.2)
Type of model	**Range used**
Blackbody (Temp., K)	20 to 160 k (steps of 1k)
Power law (slope)	-2.0 to -1.0 (steps of 0.05)
BPASS (logAge, yr)	6.0 to 8.9 (steps of 0.1)

APPENDIX C: VARIABILITY IN ULTRAVISTA

C1 Public catalogues

In order to understand the flux differences in the *J* band for CR7 for different public UltraVISTA DRs (McCracken et al. 2012), we check how the magnitude of CR7 has changed in the three DRs of the UltraVISTA survey. We retrieve public catalogues from the ESO archive and include all sources that are (i) detected in all UltraVISTA DRs and (ii) are within 5 arcmin separation from CR7. CR7 itself is only detected in all three releases in the *Y* and *J* bands and thus we focus on these bands. DR1 was released in 2012 February, while DR2 was released in 2014 January and DR3 in 2016 April. While DR1 has an average exposure time of $\sim$50 ks (including the deep stripes), the DR2 exposure time at the location of CR7 is 46 ks. DR3 does not seem to have added any exposure time to the region where CR7 is found, with DR3 listing a total exposure time of 44.6 ks, down from 46 ks in DR2. We use aperture photometry in 1 and 2 arcsec and mag-auto provided in the public

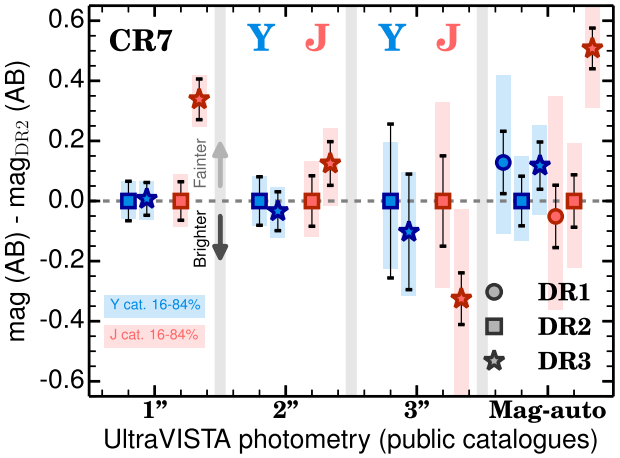

Figure C1. Comparison between *Y* and *J* AB magnitudes in public UltraVISTA catalogues for DR1, DR2, and DR3. We study the potential variation in relation to DR2 (used in S15) for magnitudes measured with apertures (diameter) of 1, 2, 3 arcsec and mag-auto. We show the errors provided in the public catalogues, but we also estimate more conservative errors by computing the 16th and 84th percentiles of the change in magnitude from one DR to the next of sources in the vicinity of CR7 with magnitudes between 23 and 25. We find no statistical significant variation in *Y*. The variations in *J* from DR2 to DR3 in both 1 arcsec and mag-auto are above 2σ.

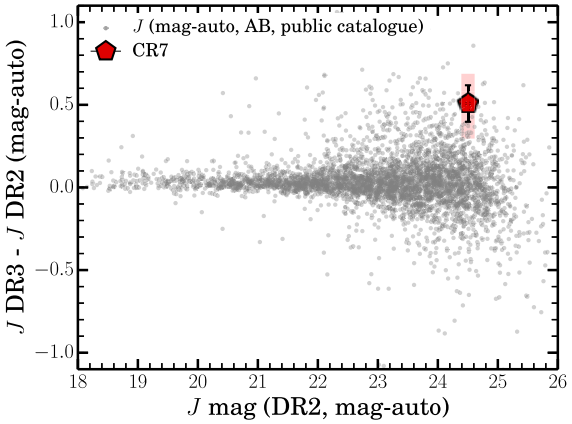

Figure C2. Comparison between mag-auto magnitudes in the public DR3 and DR2 UltraVISTA *J* catalogues. We show CR7 and also all matched sources between DR2 and DR3 that are within 5 arcmin of CR7. The quadrature combined photometric error of DR2 and DR3 implies that the change in mag-auto for CR7 is statistically significant by $\approx 4.6\sigma$, but we note that there are a few other sources for which this change in magnitude also happens. Motivated by this, we derive a more conservative error, based on the 16th and 84th percentiles of all magnitude changes between DR2 and DR3 for sources near CR7, yielding a change from DR2 to DR3 of $+0.51^{+0.14}_{-0.17}$ mag, suggesting a 3σ variation, based on the public catalogues.

catalogues and show the results in Figs C1 and C2. The quadrature combined photometric error of DR2 and DR3 would imply that the change in mag-auto for CR7 is statistically significant at a $\approx 4.6\sigma$ level. However, we find a few other sources in the public catalogue for which such change in magnitude also happens. Furthermore, we derive a more conservative error, based on the 16th and 84th percentiles of all magnitude changes between DR2 and DR3 for sources in the vicinity of CR7, yielding a change from DR2 to DR3 of $+0.51^{+0.14}_{-0.17}$ mag in *J* mag-auto. Using the public catalogue,

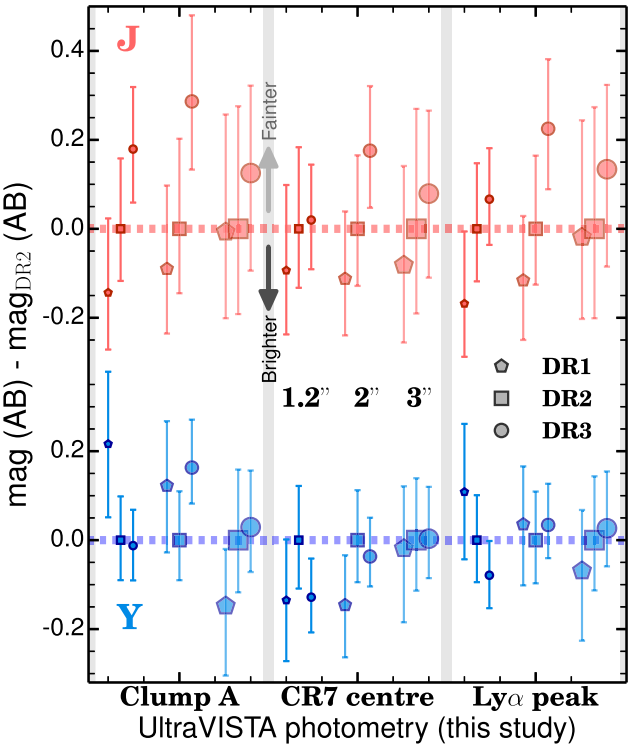

Figure C3. The difference in magnitude when compared to measurements of DR2 from the different UltraVISTA DRs. We measure magnitudes with apertures (diameter) of 1.2, 2.0, and 3.0 arcsec centred on clump A, on the centre of the three clumps and on the peak of Ly α emission for *Y* and *J* and compare them with the same measurement for DR2. We find no statistically significant variation from the different DRs, with only tentative dimming in the *J* band from DR1 to DR2 and DR3.

this implies a 3σ statistical significance for the *J* band. However, as Fig. C1 shows, the mag-auto variation seems to be the most extreme, and variations in the *J* band for aperture photometry are less significant, except for 1 arcsec.

A variation of $+0.51^{+0.14}_{-0.17}$ mag (becoming fainter) in the *J* band is a significant change in the public catalogue ($\approx 3\sigma$), and dramatically affects the interpretation of a high EW emission line in the *J* band which was taken as a strong prior in S15. However, we caution that even though we use conservative errors based on the public catalogue (the formal errors would imply a change closer to 5σ), we find that there are a few other sources with a similar magnitude change in the vicinity of CR7 (see Fig. C2). We are therefore cautious in interpreting this change in magnitude as intrinsic variability of CR7 using the public catalogues. For the *Y* band for example, we find no evidence for variability within the 1σ uncertainties. For more detailed results, see Figs C1 and C2.

C2 Public images/data

We use the ESO archive to obtain the reduced DR1, DR2, and DR3 UltraVISTA mosaics in *Y*, *J*, *H*, and *K*. We make cut-outs of all images centred on CR7 and assure that they are well aligned. We perform aperture photometry on the positions defined in Fig. 1 for all bands and for all DRs. In order to estimate the error, we use SExtractor (Bertin & Arnouts 1996) to produce a segmentation map and place 1000 apertures with the same size in empty regions in the image and then compute the 16th and 84th percentiles as our errors. We also compute the median of all empty apertures

and subtract it before computing the flux or magnitude for a given aperture, in order to subtract the local sky/background. We note that CR7 is in the transition between shallow and deeper Ultra-VISTA data. Due to this, we concentrate our analysis in a region of ≈30 arcsec × 30 arcsec and measure the local noise in this region. In order to correct our aperture photometry measurements, we follow Bowler et al. (2017b) and apply the necessary corrections.[9]

APPENDIX D: VARIABILITY IN *HST* PHOTOMETRIC DATA

In order to measure or constrain any potential variability of CR7, as whole or in individual UV clumps, we use *HST* data taken on 2012 March 02, which was presented and explored in S15 (*HST* Program 12578), but we also use recent public data taken on 2017 March 14 (*HST* program 14596). For both *HST* programs, filters F110W and F160W were used. We first register a 30 arcsec × 30 arcsec cut-out of the four available stacks assuring that all sources within the image are fully aligned. We then use ZP = 26.6424 and 25.7551 for F110W and F160W,[10] respectively. We measure the flux and AB magnitudes in both filters for both dates, with apertures varying from 0.2 to 3 arcsec in steps of 0.1, centred on the UV centroid of clumps A, B, and C based on the stack of 2012 and 2017 data, and also centred on the rough centre of the full system (Fig. 1). In order to correct the 2σ aperture magnitudes, we apply corrections for the missed flux of point sources, which vary from ≈0.6 to 0.7 for the smallest apertures to ≈0.95 for the largest.[11] In order to estimate the magnitude errors for a specific aperture and to measure a specific clump/location, we place 1000 empty apertures throughout the image, avoiding bright sources (exploring a segmentation map produced with SExtractor) and compute the 16th and 84th percentiles, which we fold through to obtain magnitude errors. We also calculate the median of the flux measured in those 1000 empty apertures and subtract it from the appropriate measurement, with the assumption that the median flux on locations without sources is a good proxy for the background at the location where we make the measurements.

APPENDIX E: SPECTROSCOPY METHODOLOGY: COMPARISON WITH OTHER STUDIES

In order to evaluate and compare our methods and results for CR7 in the context of the discussions in this paper and e.g. Shibuya et al. (2018a), we use X-SHOOTER data for recent studies. We explore other sources with detected emission lines at $z \sim 7$–8 that are publicly available. These are very helpful to compare the results from different statistical analysis and to also compare the reproducibility of results. We use recent very deep follow-up observations that have detected multiple lines (Laporte et al. 2017a,b) with X-SHOOTER targeting four different $z \sim 6$–8 sources (which have also been discovered or studied by other authors, e.g. Stark et al. 2017; Smit et al. 2018). We follow the procedure presented in Sobral et al. (2018b) and used in this paper. We focus on how well we recover the different rest-frame UV lines and how the S/N we measure compares with those reported in the literature.

For CR7, we have extracted the 1D spectra at the expected (centre) position of CR7 in the VIS arm by checking it matches with the rough peak of Lyα emission in the spatial direction. For the NIR arm, we extract the 1D along the central pixel for OB1 and OB2 where we do not find any emission line in the 2D, while for OB3, we extract +3 pixels away from the centre, extracting over ±1 arcsec in the VIS and NIR arms (±8 to ±4 pixels depending on the arm). We follow the same methodology for the other X-SHOOTER spectra we study, taking care to extract over the signatures identified in the papers presenting the data and we extract over ±6 spatial pixels in the VIS arm and ±3 spatial pixels in the NIR arm to account for the fact that sources are typically more compact than CR7.

As for our main analysis of CR7, we start by using the errors provided by the pipeline reduction, but also investigate the S/N distribution across each X-SHOOTER arm. We find that the noise is typically overestimated for our extractions based purely on the pipeline noise by factors of about 1.1 in the VIS arm and factors from 1.4 to 1.1 in the NIR arm (see also e.g. Zabl et al. 2015). We remeasure the noise and check that the S/N of extracted spectra without any expected signal resemble Gaussian distributions. By using the pipeline noise directly, we find that the S/N of empty regions is underestimated, but our final noise estimates yields a Gaussian S/N distribution for extractions consistent with no extragalactic signal.

Our re-analysis of data from the literature is able to recover spectra that resemble those in the literature. For Lyα emission, we agree with three-fourth detections, although we tend to find slightly lower S/N for those lines and also note that such Lyα lines (e.g. COSY) are actually very narrow. However, for other lines, out of four reported detections we only recover two lines at an S/N > 2.5. This means that two of the lines reported to be at the $\approx 4\sigma$ level in the literature, are found to be below $<2.5\sigma$ in our MC analysis. This is similar to the decreased significance between our study and S15 for HeII in CR7, and it is likely a direct consequence of how the noise/significance is measured, along with effects of smoothing/binning. We show examples in Figs E1 and E2. Here, we list the results for the sources investigated:

(i) COSY (Laporte et al. 2017b): We confirm Lyα at $z = 7.1542^{+0.0007}_{-0.0009}$, in full agreement with what had been found by Stark et al. (2017) with a MOSFIRE spectrum and what is also concluded in Laporte et al. (2017b). However, we note that contrarily to the discussion presented in Laporte et al. (2017b), we find that COSY's Lyα line is not unusually broad, but rather relatively narrow for an Lyα line (see also Fig. E2). We find that its FWHM (deconvolved for resolution) is 312^{+27}_{-32} km s^{-1}, and thus consistent with being as narrow as the Lyα line from CR7. COSY's Lyα line is very narrow given how bright in the rest-frame UV this source is, but this seems to be a general feature of Lyα emitters in the epoch of re-ionization (see Matthee et al. 2017a; Sobral et al. 2018b). Apart from Lyα, we find no other emission line in COSY in the X-SHOOTER spectra above 2.5σ. The reported detections of NV and HeII at $\approx 4\sigma$ are all below 2.5σ in our analysis. Specifically, we find that the reported NV detection is consistent with the noise level and the proximity to a strong OH line. For HeII, while there is a tentative signal (see Fig. E1), the peak of the signal is too narrow, while the full signal is not significant. The potential HeII signal for COSY, if measured manually (as our automated analysis does not detect it), would be consistent with a very low FWHM of ≈50 km s^{-1}, below the resolution. We note that Laporte et al. (2017b) also present a

[9] We assume that our apertures of 1.2, 2.0, and 3.0 arcsec in [*Y*, *J*, *H*, *K*] recover [0.56,0.6,0.63,0.64], [0.79,0.83,0.85,0.87], and [0.92,0.94,0.95,0.96] of the total flux, respectively.

[10] Zero-points are found in: http://www.stsci.edu/hst/wfc3/analysis/ir_phot_zpt.

[11] We use the corrections provided in: http://www.stsci.edu/hst/wfc3/analysis/ir_ee.

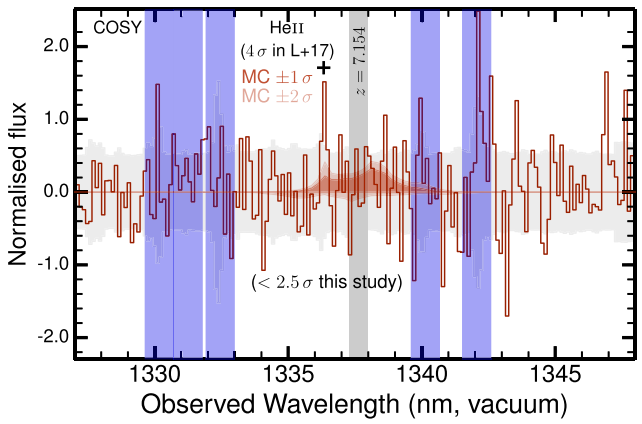

Figure E1. Our analysis applied to COSY (Stark et al. 2017) and its potential HeII line detection in X-SHOOTER data (Laporte et al. 2017b). We show the extracted 1D spectrum binned by one-third of the resolution and also highlight the position of OH lines. Shaded regions show the $\pm1\,\sigma$ errors (grey) and the range of MC fits within 1σ and $2\,\sigma$, following Fig. 6. We identify the signature identified as HeII in our 1D and indicate it with a $+$. However, we find that such tentative signal corresponding to a redshift of $z \approx 7.15$, reported to have a significance of $\approx 4\sigma$ in Laporte et al. (2017b) is below 2.5σ in our forward-modelling MC analysis.

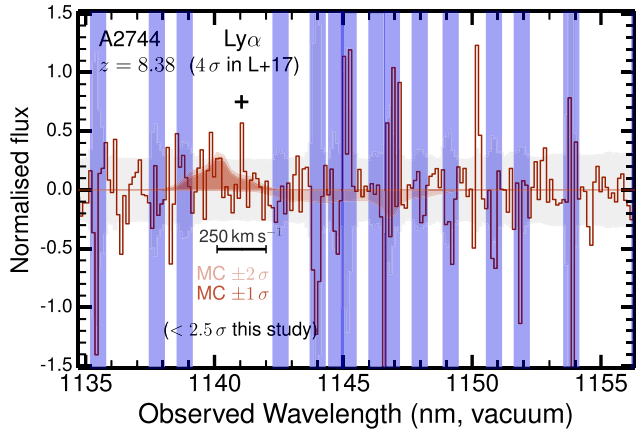

Figure E2. Our analysis applied to A2744 and its potential Lyα line detection in X-SHOOTER data (Laporte et al. 2017a). We show the extracted 1D spectrum binned by one-third of the resolution and also highlight the position of OH lines. We recover and indicate the signal interpreted as Lyα in Laporte et al. (2017a) with a $+$. The potential line is reported to have a significance of 4σ in Laporte et al. (2017a), but our methodology implies that any signal is below a significance of $2.5\,\sigma$. Furthermore, we also indicate the expected width of a very narrow Lyα line with an FWHM of 250 km s^{-1}, which is significantly broader than the single spectral element identified as an emission line in Laporte et al. (2017a).

MOSFIRE spectrum that seems find HeII for COSY, but here we focus on X-SHOOTER and we aim to only report our findings in our framework.

(ii) COSz1 (Laporte et al. 2017b): we recover the CIII]1909 emission line above 3σ (3.4σ). The detection of the line is consistent with Laporte et al. (2017b), despite our detection at lower significance (3.4σ instead of 4σ), but the difference is small. We also note that for CIII], Laporte et al. (2017b) seem to have binned the spectra at least to a fraction of the resolution; while that is not always the case for the other lines, and particularly not the case for the lines in other sources which we find to be below 2.5σ and below the resolution of the instrument. Apart from CIII], no other emission line is found in our analysis above 2.5σ, which is in agreement with Laporte et al. (2017b).

(iii) COSz2 (Laporte et al. 2017b): We confirm Lyα and no other emission lines from this source above 2.5σ in our analysis, in full agreement with Laporte et al. (2017b). Due to the overlap with a strong OH line, we find that the Lyα line is detected at just below 3σ; Laporte et al. (2017b) report its significance as $\approx 3\,\sigma$, and thus we conclude there is good agreement. Furthermore, we identify a significant emission line at $\approx$1552 nm, also in full agreement with Laporte et al. (2017b), which is argued in that paper to be from a source at $z \sim 2$ and to potentially be [OIII]5007, since it does not match any potential line for the redshift of COSz2.

(iv) A2744 (Laporte et al. 2017a): we find no emission lines detected above 2.5σ on the entire X-SHOOTER spectra. In particular, while we can tentatively identify the signal of the reported 4σ detection of Lyα in the 2D spectrum and explicitly extract the spectrum centred on that, our analysis reveals it is not statistically significant; see Fig. E2. We find that the signal in Laporte et al. (2017a) comes from too few pixels and is below the resolution, implying an FWHM of ≈ 20 km s^{-1}. Given that the resolution, measured with nearby sky lines on the spectrum, is close to 60 km s^{-1}, a potential emission line with an FWHM of ≈ 20 km s^{-1} is below the resolution. This means that this line would have an FWHM about three times lower than the OH lines; this is something more typical of noise and/or artefacts, as any real line will have at least an FWHM equal to the resolution, even if intrinsically it is even narrower. We therefore conclude that with our conservative statistical analysis that we apply to CR7, what is measured as a $4\,\sigma$ Lyα line in Laporte et al. (2017a) for A2744 is consistent with noise or an artefact and it is below $2.5\,\sigma$ in our framework, and thus we would report it as undetected. In Fig. E2, we also show how a very narrow Lyα line with an FWHM of 250 km s^{-1} should look like in the spectrum, significantly broader than the potential line indicated with $+$.

This paper has been typeset from a TEX/LATEX file prepared by the author.